An Isolated Multiport DC-DC Converter for Integrated Electric Vehicle On-board Charger

Ioannis Kougioulis, Anirban Pal, *Student Member, IEEE*, Patrick Wheeler, *Fellow, IEEE*, and Md Rishad Ahmed, *Member, IEEE*

***Abstract*—This paper proposes an integrated on-board charger (IOBC) for Electric Vehicles (EVs) based on an isolated three-port DC-DC converter. The proposed architecture integrates the on-board charger (OBC) and the auxiliary power module (APM) in a single multiport converter, offering low component count. The proposed converter is capable of charging high-voltage (HV) and low-voltage (LV) batteries simultaneously, over the entire battery voltage ranges. A three-winding transformer is used to provide galvanic isolation between the converter ports and consequently, power flow is coupled among the three ports. In this paper, a boundary condition is derived for the first time and a novel modulation scheme is proposed to regulate the power flow at the HV and LV ports independently, utilizing the converter's 3-degrees-of-freedom (DOF). Hence, charging of the HV and LV batteries can be realized similar to dual-active-bridge (DAB) and phase-shifted full-bridge (PSFB) converter, respectively. Results show that all converter semiconductor devices operate with zero-voltage-switching (ZVS) over wide power and voltage range without the need of additional resonant components, due to the proposed 3-DOF selection scheme. A 3.5kW hardware prototype of the proposed converter is built and tested and key experimental results are presented to verify the converter theoretical analysis and ZVS operation.**

***Index Terms*—Integrated electric vehicle (EV) charger, low-voltage (LV) DC-DC converter, dual-active-bridge (DAB) converter, phase-shifted full-bridge (PSFB), three-port converter.**

I. Introduction

DUE to the growing concern about climate change, electric vehicles (EVs) are gaining popularity and gradually replacing the fossil fuel-based transportation solutions. Conventionally, EVs have an on-board charging system which is plugged into the utility grid to charge the on-board high-voltage (HV) batteries that power the electric motor. Moreover, EVs are equipped with a low-voltage (LV) battery that supplies auxiliary loads e.g., lights, communication and navigation systems. Current practice suggests that the on-board charging system has a front-end active power-factor-correction (APFC) stage followed by two separate DC-DC units i.e., on-board charger (OBC) and auxiliary power module (APM), which are responsible for charging the HV and LV batteries, respectively [1], [2]. Fig. 1 presents the schematic diagram of a conventional OBC and APM architecture.

A topological integration of the OBC and APM can significantly reduce the total weight, volume, and cost of the EV charger, save space and extend the driving range capability of the EV [3]. In addition, the integrated charger can achieve high-efficiency, as the number of series connected power processing stages are reduced, along with the reduction of magnetic components. The schematic diagram of an integrated on-board charger (IOBC) is presented in Fig. 2.

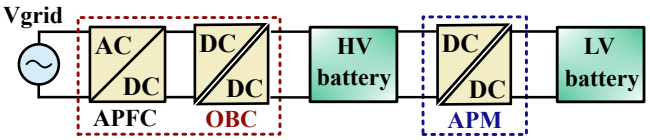

Fig. 1. Schematic diagram of conventional OBC-APM architecture.

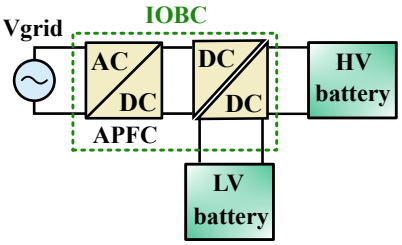

Fig. 2. Schematic diagram of an integrated OBC-APM charger.

The front-end AC/DC power-factor-correction (PFC) stage is responsible for the active power decoupling (APD) and is the same for both the conventional and the integrated charger architecture. However, in the integrated charger a multiport DC/DC converter is used to regulate the charging power of the HV and LV batteries, compared to the two separate DC/DC units of the conventional OBC-APM architecture.

An integrated charger can support several charging functions, including HV to LV battery charging when the EV is running, as well as simultaneous HV and LV battery charging from the grid when the EV is parked [4]. Recently, simultaneous charging of the HV and LV batteries from the grid is attracting interest, as it can allow improved functionalities, for example, by enabling battery pre-conditioning [4]. Moreover, during OBC operation the LV battery provides continuous power to the battery control modules, instrument panel and mobile devices thus, simultaneous charging of both batteries is necessary to avoid draining of the LV battery [5].

The integrated charger topologies reported in [6]–[10] combine the active power decoupling and the LV battery charging circuits, consequently, reducing the number of the semiconductor components, as well as the size of the DC-link capacitors. However, simultaneous charging of the HV and LV batteries is not possible. Moreover, mechanical switches are utilized to configure the circuit for either HV or LV battery charging, resulting in low system reliability. [11] proposed an

improved architecture with simultaneous HV and LV battery charging capability, however, mechanical switches are still necessary to switch between each charging function. Furthermore, an additional LC resonance circuit is required to achieve simultaneous charging of the HV and LV batteries, increasing the converter component count. The integrated converter in [12] can charge HV and LV batteries simultaneously, utilizing a selective switch and two resonant tanks, but fails to meet isolation requirements between the HV battery and the grid. [13] proposed a novel integrated converter based on the phase-shifted full-bridge (PSFB) and LLC resonant converter, with simultaneous HV and LV battery charging operation. However, two separate two-winding transformers are necessary to interface the HV battery and the grid, as well as the HV and the LV battery, increasing the volume of the converter.

Several integrated chargers proposed in recent literature focus on combining the transformers of the OBC and APM units using a single multiwinding transformer [14]–[18]. Although the converter demonstrated in [14] utilizes a single three-winding transformer, it suffers from reduced efficiency due to the additional buck converter at the LV battery port. [15] proposed an integrated charger based on the triple-active bridge (TAB) converter, however, special transformer design is required to minimize the leakage inductance and to decouple the power flow between the three ports. In [16], a TAB converter is used as an integrated charger and an optimal modulation strategy is employed to minimize the conduction loss of the converter. However, control complexity of the converter is significantly increased due to the 12 active semiconductor devices and the coupled power flow between the three ports. A dual-output resonant DC-DC converter with reduced size and increased efficiency has been presented in [17] however, simultaneous charging of the HV and LV batteries is not discussed. Finally, the high-power current-fed triple-active bridge (CF-TAB) converter presented in [18] demonstrates extended zero-voltage-switching (ZVS) characteristics for IOBC, however, additional coupled inductors are required before the HV and LV batteries, which increase the volume of the converter.

Multiport converters are promising for IOBC application, since they can significantly reduce the total number of semiconductor components of the integrated charger. Moreover, in multiport converters a single multiwinding transformer can be utilized and thus, overall volume, weight and cost of the integrated charger are reduced, while at the same time efficiency is improved. However, the main challenge of this architecture results from the use of the multiwinding transformer and the fact that power flow is coupled between the converter ports [19]. The TAB multiport converter has attracted significant interest and has been initially presented as an extension of the dual-active-bridge (DAB) topology, utilizing phase-shift and duty ratio control [20]. In addition, [21] presented a multivariable modulation scheme aiming to improve the effiency of TAB converter, especially at light load conditions, while [22] proposed a power flow control technique based on a frequency division method. Furthermore, [23] presented a variation of the conventional TAB converter, by adding two resonant LC tanks, aiming to extend the soft-switching range of TAB, due to the series-resonant (SR) converter operation. However, none of the TAB converters presented in [20]–[23] is suitable for IOBC application, since they account for increased number of active semiconductor devices, control complexity, volume and cost. A three-port DC-DC converter with reduced number of active switches was presented in [24], however, specialized transformer design with low primary winding leakage inductance is required to decouple the power flow between the three ports. Moreover, an additional LC resonant tank is utilized, which increases the component count of the converter. Finally, a resonant three-port converter was proposed in [25] and demonstrates extended soft-switching characteristics. However, the two additional LCC and LC resonant tanks increase the component count and volume of the converter significantly.

This paper proposes an isolated three-port DC-DC converter topology, which combines the two DC-DC converters of the OBC and APM units. The proposed converter has the following features. (a) The three-port converter ensures isolation between the HV battery and the grid, as well as between the HV and LV batteries. A single three-winding transformer is utilized, which results in reduced weight, volume and cost of the magnetic components, compared to the use of two separate two-winding transformers. (b) The HV battery is interfaced to a bidirectional voltage port, while the LV battery is connected to a unidirectional current port. (c) The proposed solution employs only eight active devices which is significantly lower than the conventional two-stage solution [26]. (d) A novel modulation strategy is proposed to control the power flow between the three ports and adjust the charging profiles of the HV and LV batteries individually. As a result of the proposed modulation scheme, power flow to the HV and LV batteries can be controlled similar to dual-active-bridge (DAB) and phase-shifted full-bridge (PSFB) converter architecture, respectively. (e) The integrated converter can charge the LV battery directly from the HV one, while also HV and LV batteries can be charged simultaneously from the grid. (f) The converter can switch between the different charging functions without the need of mechanical switches or relays. (g) The proposed converter can operate over the entire voltage range of the HV and LV batteries. (h) All active semiconductor switches can operate with ZVS over a wide power and voltage range without the need of additional resonant components, due to the proposed converter 3-degrees-of-freedom (DOF) operation and 3-DOF selection scheme.

This article is organized as follows. Section II presents the topology of the proposed converter and its operating principles. In this section, analytical equations are derived, the converter ZVS capability is explored and the proposed 3-DOF selection scheme is presented. In addition, Section II describes the proposed HV and LV battery charging strategy. Simulation results of the converter operation are shown in Section III. Section IV provides experimental results to further validate the theoretical analysis and the converter operation. Section V presents the efficiency of the proposed converter, including a loss breakdown analysis. The proposed converter topology is then compared with the existing integrated charger solutions in Section VI. Finally, Section VII concludes the presented work.

II. Converter Operation And Analysis

A. Converter topology and charging functions

The proposed three-port DC-DC converter topology is shown in Fig. 3. A three-winding high-frequency (HF) transformer with turns ratio $n_1 : n_2 : n_3$ is used to provide galvanic isolation between the ports. Port 1 is connected to the utility AC grid through a front-end PFC stage. Hence, the input DC voltage of port 1 i.e., V_{DC}, is considered well-regulated and the PFC stage is not discussed in this paper. Ports 2 and 3 are connected to the HV and LV batteries with voltage levels V_{HV} and V_{LV}, respectively. In addition, L_1, L_2 and L_3 represent the leakage inductance of the transformer primary, secondary and tertiary winding, respectively. The transformer magnetizing inductance is significantly higher compared to the leakage inductance of each winding and magnetizing current is negligible. Therefore, magnetizing inductance is not considered in the converter topology of Fig. 3.

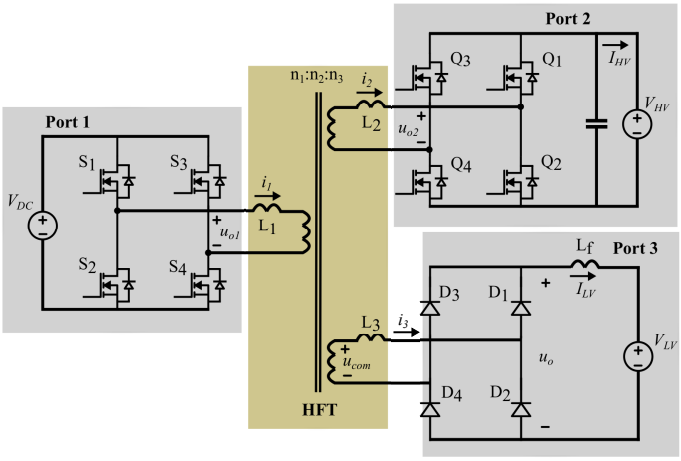

Fig. 3. Proposed integrated converter topology.

In the case of ports 1 and 2, H-bridge converters are utilized to interface each port with the three-winding transformer. Hence, port 1 and port 2 operate as voltage ports and have bidirectional power flow capability. Each H-bridge converter generates a high frequency quasi-square wave voltage, denoted as u_{o1} and u_{o2} for port 1 and 2, respectively. Port 3 is connected to a diode bridge rectifier through an output filter inductor (L_f) and thus, port 3 operates as a unidirectional current port. The proposed converter can be represented by an equivalent circuit model shown in Fig. 4, where again the converter magnetizing inductance is omitted.

For the equivalent circuit model of Fig. 4 the following have been considered. (a) The three-winding transformer has been replaced by its equivalent lossless model i.e., resistance of the transformer windings is neglected. (b) The output filter inductor of port 3 i.e., L_f, is chosen large enough to have negligible ripple in the output current i.e., I_{LV}. Hence, port 3 can be represented as a square wave current port with amplitude I_o, due to the diode bridge action. (c) The transformer tertiary winding leakage inductance i.e., L_3, has been directly neglected to simplify analysis, similar to PSFB converter analysis [27]. More specifically, due to the square waveform

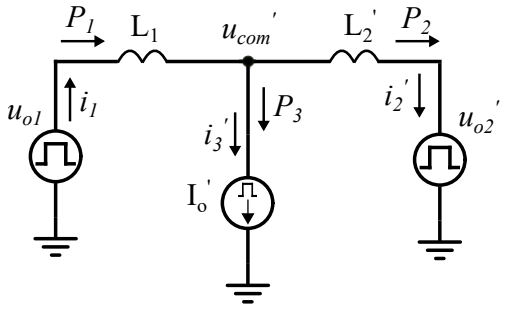

Fig. 4. Equivalent circuit model of the proposed integrated converter.

of the tertiary winding current i.e., i_3, L_3 is only affecting the circuit operation when i_3 is changing polarity and results in the commutation effect in the diode bridge of port 3. However, L_3 is considered small and current commutation time is negligible and thus, L_3 can be omitted from the equivalent circuit of Fig. 4. (d) All parameters are referred to the primary side of the transformer i.e., $u'_{o2} = (n_1/n_2)u_{o2}$, $i'_2 = (n_2/n_1)i_2$, $L'_2 = (n_1/n_2)^2 L_2$, $i'_3 = (n_3/n_1)i_3$, $L'_3 = (n_1/n_3)^2 L_3$.

Due to the use of the multiwinding transformer, the power flow equations for this converter are mutually coupled, and control complexity is increased [28]. In this paper a novel modulation strategy is proposed to control power flow at ports 2 and 3. Power flow between port 1 and 2 can be controlled similar to a DAB converter, whereas power flow to port 3 can be controlled using PSFB converter control. The proposed modulation scheme is essential for simultaneous charging of the HV and LV batteries and to ensure independent control on charging of each battery. The detailed operation of the converter is presented in sub-section II-B.

Fig. 5 presents the charging functions of the proposed integrated charger. In the first function, the EV is not connected to the grid and the LV battery can be charged from the HV battery. In this function, the operation is similar to a conventional PSFB converter [29]–[31]. In the second charging function, the EV is connected to the grid and the HV and LV batteries can be charged simultaneously. This paper focuses on the second charging function i.e., simultaneous charging of the HV and LV batteries from the grid. However, experimental results of the converter PSFB operation are also presented to demonstrate the performance of the proposed integrated charger during HV to LV charging function (Section IV).

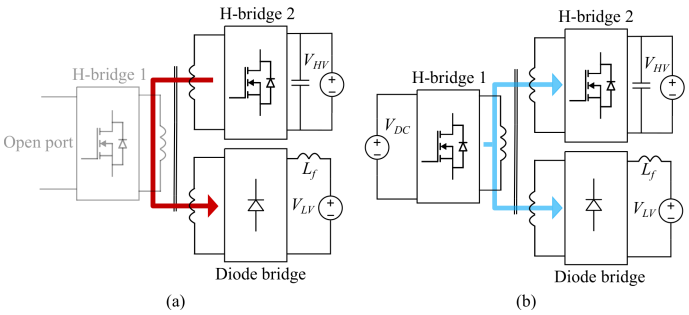

Fig. 5. Charging functions of the proposed integrated charger i.e., a) HV to LV battery charging and b) simultaneous HV and LV battery charging from the grid.

B. Converter steady state analysis and modulation scheme

The gate signals of the semiconductor switches of the primary and secondary H-bridge converter are shown in Fig. 6a. The applied voltages at the transformer primary and secondary winding i.e., u_{o1} and u_{o2}, are generated according to these gate signals and they are presented in Figs. 6b-c, along with the current waveforms of the primary and secondary transformer windings i.e., i_1 and i_2. Voltage induced at the low voltage winding of the transformer i.e., u_{com}, and the respective winding current i.e., i_3, are shown in Fig. 6d. The phase-shift between the fundamental components of u_{o1} and u_{o2} is denoted as ϕ, while τ_1 and τ_2 are the pulse widths of the applied voltages u_{o1} and u_{o2}, respectively. As shown in Figs. 6b-c, the proposed converter offers 3-degrees-of-freedom (DOF) i.e, ϕ, τ_1 and τ_2.

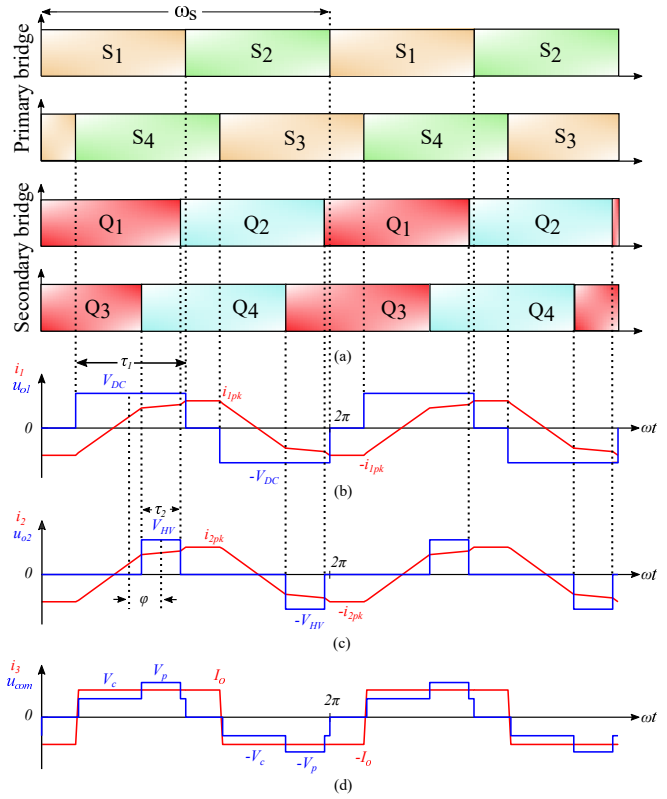

Fig. 6. a) Gate signals of semiconductor switches $S_1 - S_4$, $Q_1 - Q_4$, b) primary, c) secondary and d) tertiary winding voltage and current waveforms with 3-DOF converter operation.

From the equivalent circuit model shown in Fig. 4, the transformer primary winding current is the summation of the primary referred secondary and tertiary winding currents i.e., $i_1 = i_2' + i_3'$. As shown in Fig. 6c, the secondary winding current i.e., i_2, has a trapezoidal shape similar to DAB converter current [32]. Moreover, the tertiary winding current i.e., i_3, is a square wave and is similar to PSFB converter current [27]. In the case of i_3, the ideal square waveform is obtained under two assumptions. (a) First, the tertiary winding leakage inductance i.e., L_3, has been neglected as shown for the equivalent model of Fig. 4. Hence, the commutation effect taking place in the diode bridge of port 3 due to L_3 is not considered. Finally, ripple in the output current i.e., I_{LV}, is considered negligible due to the large output filter inductor i.e., L_f.

Fig. 6d shows that u_{com} is a multilevel waveform which results from the superposition of the applied voltages at the primary and secondary winding of the transformer at each time instant. Applying the superposition theorem on the equivalent circuit model of Fig. 4, u_{com} referred to primary i.e., u_{com}', can be expressed as follows

$$u_{com}'(t) = \frac{L_2'}{L_1 + L_2'} u_{o1}(t) + \frac{L_1}{L_1 + L_2'} u_{o2}'(t) \tag{1}$$

Fig. 7 presents the induced voltage at the transformer tertiary winding with respect to primary i.e., u_{com}', for two different cases i.e., Case I and Case II, where variations of ϕ, τ_1 and τ_2 have been considered.

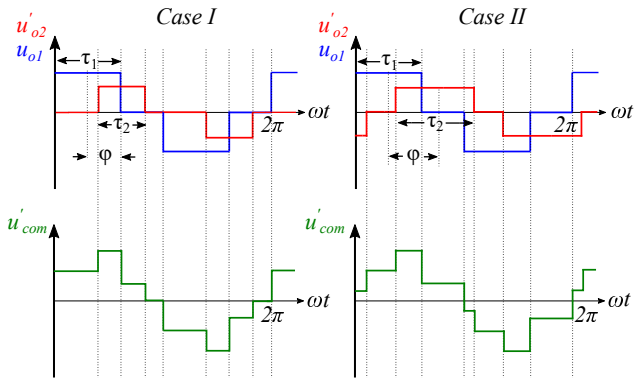

Fig. 7. Tertiary winding induced voltage referred to primary i.e., u_{com}', for two different cases of u_{o1} and u_{o2}'.

Case I and Case II operation are presented in Fig. 7 assuming $V_{DC} > (\frac{n_1}{n_2})V_{HV}$, however, the classification in the two cases is independent of u_{o1} and u_{o2}' amplitudes. More specifically, the relationship between the converter's 3-DOF i.e., ϕ, τ_1 and τ_2 determines Case I or Case II operation and the boundary condition is given below

$$\phi + \frac{\tau_1}{2} + \frac{\tau_2}{2} \leq \pi \tag{2}$$

The proposed converter operates in Case I when the boundary condition in (2) is satisfied, otherwise the converter operates in Case II.

The diode bridge of port 3 rectifies u_{com} and the expression of the average output voltage of port 3 i.e., V_{LV}, is given below for each case of Fig. 7.

$$Case\ I: V_{LV} = \frac{n_3}{n_1}\frac{2L_2'}{L_1 + L_2'} d_1 V_{DC} + \frac{n_3}{n_2}\frac{2L_1}{L_1 + L_2'} d_2 V_{HV} \tag{3}$$

$$Case\ II: V_{LV} = \frac{n_3}{n_1}\frac{2L_2'}{L_1 + L_2'} d_1 V_{DC} + \frac{n_3}{n_2}\frac{2L_1}{L_1 + L_2'} y V_{HV} \tag{4}$$

where $d_1 = \frac{\tau_1}{2\pi}$, $d_2 = \frac{\tau_2}{2\pi}$ and $y = (1 - d_1 - \frac{\phi}{\pi})$. The 3-DOF i.e., ϕ, τ_1 and τ_2 can be selected in the range of $0 < \phi \leq \frac{\pi}{2}$, $0 < \tau_1 \leq \pi$, $0 < \tau_2 \leq \pi$ and consequently, $0 < d_1 \leq 0.5, 0 < d_2 \leq 0.5$.

Equations (3), (4) show that in the first case, mean output voltage is a function of τ_1 and τ_2 i.e., $V_{LV} = f(\tau_1, \tau_2)$, while in the second case $V_{LV} = f(\tau_1, \phi)$. In this paper, Case I operation is preferred so that V_{LV} is independent of ϕ and can be regulated using only τ_1 and τ_2, similar to duty cycle control of PSFB converter. As a result, ϕ can be utilized to control power flow between port 1 and 2 as in DAB converter.

To determine the power flow in the proposed converter, first, the transformer primary and secondary winding voltages i.e., u_{o1} and u_{o2}, are expressed using Fourier series [33]

$$v_{o1}(t) = \sum_{n=1,3,5..}^{\infty} \frac{4V_{DC}}{n\pi} cos(\frac{n\alpha_1}{2}) sin(n\omega_s t) \tag{5}$$

$$v_{o2}(t) = \sum_{n=1,3,5..}^{\infty} \frac{4V_{HV}}{n\pi} cos(\frac{n\alpha_2}{2}) sin(n\omega_s t + n\phi) \tag{6}$$

where $\alpha_1 = \pi - \tau_1$, $\alpha_2 = \pi - \tau_2$, $\omega_s = 2\pi f_s, f_s$ is the converter's switching frequency and n indicates the order of harmonic components. The equivalent model of Fig. 4 is then utilized to derive the power flow equations as given below [34]

$$P_1 = P_2 + P_3 \tag{7}$$

$$P_2 = \sum_{n=1,3,5..}^{\infty} \frac{8V_{DC}V'_{HV} cos(\frac{n\alpha_1}{2}) cos(\frac{n\alpha_2}{2})}{\pi^2 n^3 X_{eq}} sin(n\phi) \tag{8}$$

$$P_3 = V_{LV} I_{LV} \tag{9}$$

where $X_{eq} = \omega_s(L_1 + L'_2)$, which represents the equivalent impedance between ports 1 and 2.

Expression (8) suggests that power at port 2 is a function of all 3-DOF i.e., $P_2 = f(\phi, \tau_1, \tau_2)$. Moreover, according to (9), the desired power at port 3 can be achieved by adjusting the respective port output voltage i.e., V_{LV}. Thus, when the converter operates as in Case I (Fig. 7), τ_1 and τ_2 can be utilized to adjust V_{LV} and control the power flow of port 3 similar to PSFB converter, while ϕ can be independently selected to regulate the power at port 2, similar to a conventional DAB converter. In contrast, when the converter operates as in Case II (Fig. 7), ϕ is utilized to adjust V_{LV} and hence, control complexity is increased.

A converter workspace of suitable $[\phi\ \tau_1\ \tau_2]$ sets satisfying (2) can be formed (Case I operation), based on the converter specifications i.e., power and voltage levels. A wide operating voltage range is considered for both the HV and the LV battery and more specifically, the HV battery voltage varies from 250V to 420V, while the LV battery operates from 8V to 16V. In addition, the nominal power for simultaneous charging operation is 3kW for the HV battery and 500W for the LV battery.

Expressions (3), (8) indicate that the converter $[\phi\ \tau_1\ \tau_2]$ workspace is related to the transformer turns ratio i.e., $n_1 : n_2 : n_3$, and the primary referred leakage inductances L_1 and L'_2. Based on the voltage range of the HV battery, the turns ratio between the primary and secondary winding can be selected in the range $0.625 \leq \frac{n_1}{n_2} \leq 1.05$ and more specifically, $\frac{n_1}{n_2} = 1$ has been chosen. The turns ratio between the primary and tertiary winding of the transformer has been selected considering the requirement to achieve a maximum voltage at port 3 equal to $V_{LV} = 16V$. In the worst case scenario where $V_{LV} = 16V$ is required, $V_{DC} = 400V$ and the HV battery voltage is at the lower limit i.e., $V_{HV} = 250V$, expression (3) can be utilized to calculate $\frac{n_1}{n_3}$, assuming $d_1 = d_{1,max} = 0.5$ and $d_2 = d_{2,max} = 0.5$. However, according to (3), the ratio between L_1 and L'_2 needs to be determined first. The operation of the proposed converter does not require any specific ratio or values of L_1 and L'_2. In addition, it is shown in sub-section II-E that the proposed converter achieves ZVS operation over wide power and voltage range due to the proposed 3-DOF selection scheme, which can be applied for any values of L_1 and L'_2. Hence, for the simplification of the analysis, $L_1 = L'_2$ is considered and as a result $\frac{n_1}{n_3} \approx 20$ is calculated from (3).

Figs. 8-10 present the converter workspace for Case I operation and different combinations of V_{HV}, V_{LV}, P_2 and P_3. More specifically, Fig. 8 shows the $[\phi\ \tau_1\ \tau_2]$ workspace as the HV and LV battery voltages vary and the power in the converter remains constant at nominal power levels, while in Fig. 9, the power of port 2 is varied for several HV and LV battery voltage levels. Finally, Fig. 10 shows the suitable converter workspace for port 3 power variation and different HV and LV battery voltages.

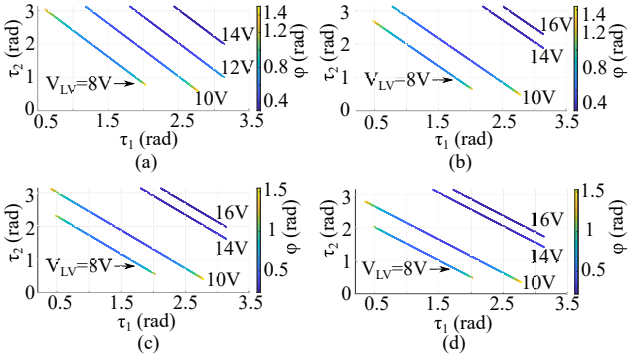

Fig. 8. 3-DOF workspace for Case I operation and LV battery voltage variation with $V_{DC} = 400V$, $P_2 = 3kW$, $P_3 = 0.5kW$, a) $V_{HV} = 250V$, b) $V_{HV} = 300V$, c) $V_{HV} = 350V$ and d) $V_{HV} = 400V$.

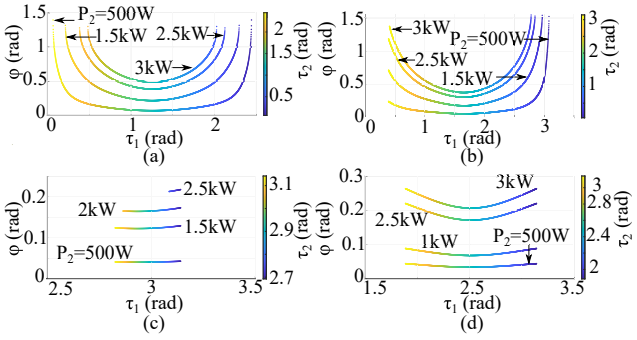

Fig. 9. 3-DOF workspace for Case I operation and port 2 power variation with $V_{DC} = 400V$, $P_3 = 0.5kW$, a) $V_{HV} = 400V$, $V_{LV} = 8V$, b) $V_{HV} = 350V$, $V_{LV} = 10V$, c) $V_{HV} = 280V$, $V_{LV} = 16V$ and d) $V_{HV} = 400V$, $V_{LV} = 16V$.

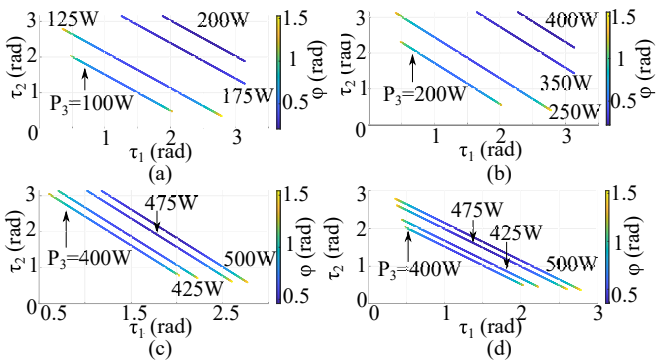

Fig. 10. 3-DOF workspace for Case I operation and port 3 power variation with $V_{DC} = 400V$, $P_2 = 3kW$, a) $V_{HV} = 400V$, $I_{LV} = 12.5A$, b) $V_{HV} = 350V$, $I_{LV} = 25A$, c) $V_{HV} = 250V$, $I_{LV} = 50A$ and d) $V_{HV} = 400V$, $I_{LV} = 50A$.

As shown in Fig. 8 the proposed converter can generate 8∼16V at port 3, covering the entire voltage range of the LV battery. When the desired output voltage increases above 10V, fewer combinations of τ_1, τ_2 can achieve the required output voltage and the $[\phi\ \tau_1\ \tau_2]$ workspace is restricted. Still, there are several combinations of 3-DOF to achieve certain output voltage and nominal power at the LV port. It is also evident from Fig. 9 that the converter can operate over the entire HV battery power range. The respective $[\phi\ \tau_1\ \tau_2]$ curves are shifted up as the power requirement at port 2 increases. This is in line with equation (8), which suggests that power flow at port 2 increases with the increase of ϕ. Finally, Fig. 10 presents the corresponding workspace of the converter over the entire LV battery power range, considering various combinations of HV battery voltage levels and LV battery current requirements. It is shown that power at the LV battery can be adjusted with various combinations of applied voltage and current, while at the same time nominal power can be delivered to the HV battery for different HV battery voltage levels.

C. Converter modes of operation

Similar to a DAB converter, the ac voltages generated at the output of each H-bridge converter i.e., u_{o1} and u_{o2}, can produce several voltage patterns, depending on the rising and falling edges of u_{o1} and u_{o2} [35]. Given that (2) needs to be satisfied (Case I operation), five modes of operation are identified which are shown in Fig. 11 for sets of ϕ, τ_1 and τ_2, corresponding to converter 3-DOF operation. The respective voltage induced at the low voltage winding of the transformer with respect to primary i.e., u'_{com}, is also shown in Fig. 11 for each mode of operation. For clarity, waveforms of Fig. 11 are drawn assuming $V_{DC} > (\frac{n_1}{n_2})V_{HV}$ for all modes of operation and $\phi > 0$ i.e., power is transferred from the grid to the HV and LV batteries. Similar waveforms can be obtained in case of $V_{DC} < (\frac{n_1}{n_2})V_{HV}$.

Table I presents the boundary conditions of the five operating modes. It can be seen that Mode I is classified into two modes i.e., Mode Ia and Ib. Although the converter operation is the same for both Mode Ia and Ib, the difference lies in the relationship between τ_1 and τ_2 i.e., $\tau_1 \geq \tau_2$ or $\tau_1 < \tau_2$. As a result, different boundary conditions describe Mode Ia and Ib.

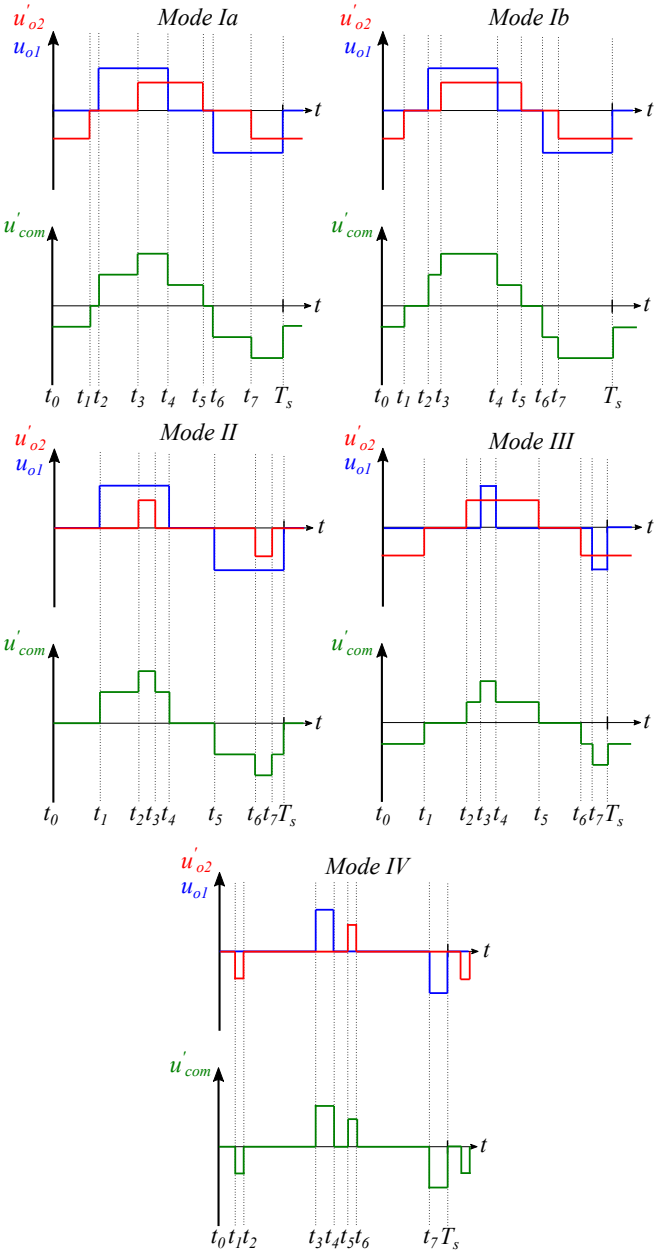

Fig. 11. Modes of operation of the proposed converter for Case I.

TABLE I
BOUNDARY CONDITIONS FOR EACH MODE OF OPERATION

Mode	Boundary conditions
Ia	$\phi > 0,\ \tau_1 \geq \tau_2,\ \phi - \frac{\tau_1}{2} + \frac{\tau_2}{2} > 0,\ -\phi + \frac{\tau_1}{2} + \frac{\tau_2}{2} > 0$
Ib	$\phi > 0,\ \tau_1 < \tau_2,\ \phi + \frac{\tau_1}{2} - \frac{\tau_2}{2} > 0,\ -\phi + \frac{\tau_1}{2} + \frac{\tau_2}{2} > 0$
II	$\phi > 0,\ \tau_1 > \tau_2,\ -\phi + \frac{\tau_1}{2} - \frac{\tau_2}{2} > 0$
III	$\phi > 0,\ \tau_1 < \tau_2,\ -\phi - \frac{\tau_1}{2} + \frac{\tau_2}{2} > 0$
IV	$\phi > 0,\ \phi - \frac{\tau_1}{2} - \frac{\tau_2}{2} > 0$

TABLE II
TIME EXPRESSIONS OF SWITCHING SUB-INTERVALS FOR EACH MODE OF OPERATION

Time instant	Mode I	Mode II	Mode III	Mode IV
t_0	0	0	0	0
t_1	$\phi - \frac{\tau_1}{2} + \frac{\tau_2}{2}$	$\frac{T_s}{2} - \tau_1$	$\phi - \frac{\tau_1}{2} + \frac{\tau_2}{2}$	$\phi - \frac{\tau_1}{2} - \frac{\tau_2}{2}$
t_2	$\frac{T_s}{2} - \tau_1$	$\frac{T_s}{2} + \phi - \frac{\tau_1}{2} - \frac{\tau_2}{2}$	$\frac{T_s}{2} + \phi - \frac{\tau_1}{2} - \frac{\tau_2}{2}$	$\phi - \frac{\tau_1}{2} + \frac{\tau_2}{2}$
t_3	$\frac{T_s}{2} + \phi - \frac{\tau_1}{2} - \frac{\tau_2}{2}$	$\frac{T_s}{2} + \phi - \frac{\tau_1}{2} + \frac{\tau_2}{2}$	$\frac{T_s}{2} - \tau_1$	$\frac{T_s}{2} - \tau_1$

TABLE III
SECONDARY WINDING CURRENT EXPRESSIONS AT SWITCHING INSTANTS IN EACH MODE OF OPERATION

Current	Mode I	Mode II	Mode III	Mode IV
$i_2(t_0)$	$-\frac{V_{DC}}{2L}\tau_1 + \frac{V_{HV}}{2L}\tau_1 - \frac{V_{HV}}{L}\phi$	$-\frac{V_{DC}}{2L}\tau_1 + \frac{V_{HV}}{2L}\tau_2$	$-\frac{V_{HV}}{L}\phi - \frac{V_{DC}}{2L}\tau_1 + \frac{V_{HV}}{2L}\tau_1$	$-\frac{V_{DC}}{2L}\tau_1 - \frac{V_{HV}}{2L}\tau_2$
$i_2(t_1)$	$-\frac{V_{DC}}{2L}\tau_1 + \frac{V_{HV}}{2L}\tau_2$	$i_2(t_0)$	$-\frac{V_{DC}}{2L}\tau_1 + \frac{V_{HV}}{2L}\tau_2$	$i_2(t_0)$
$i_2(t_2)$	$i_2(t_1)$	$\frac{V_{DC}}{L}\phi - \frac{V_{DC}}{2L}\tau_2 + \frac{V_{HV}}{2L}\tau_2$	$i_2(t_1)$	$-\frac{V_{DC}}{2L}\tau_1 + \frac{V_{HV}}{2L}\tau_2$
$i_2(t_3)$	$\frac{V_{DC}}{L}\phi - \frac{V_{DC}}{2L}\tau_2 + \frac{V_{HV}}{2L}\tau_2$	$\frac{V_{DC}}{L}\phi + \frac{V_{DC}}{2L}\tau_2 - \frac{V_{HV}}{2L}\tau_2$	$\frac{V_{HV}}{L}\phi - \frac{V_{DC}}{2L}\tau_1 + \frac{V_{HV}}{2L}\tau_1$	$i_2(t_2)$

A piece-wise time domain analysis for the five operating modes is carried out and analytical expressions of the transformer currents are derived. The duration of each sub-interval of the five operating modes is listed in Table II, utilizing the converter's 3-DOF. Analytical expressions of the transformer secondary winding current i.e., i_2, at different switching instants are given in Table III, where $L = L_1 + L_2'$. Transformer primary winding current can be estimated by applying Kirchhoff's Current Law (KCL) at the equivalent circuit of Fig. 4 i.e., $i_1 = i_2' + i_3'$. Table IV presents the primary winding currents by combining port 3 current amplitude i.e., I_o, and the secondary winding currents of Table III. Time and current expressions of Tables II-IV are presented only for half-switching period ($t_4 = \frac{T_s}{2}$) due to the symmetric operation of the converter i.e., $t_{i+4} = t_i + \frac{T_s}{2}$ and $i_2(t_{i+4}) = -i_2(t_i)$, where $i = 0, 1, 2, 3$. Finally, Table V lists the devices and their turn-on instances for different operating modes.

TABLE IV
PRIMARY WINDING CURRENT EXPRESSIONS AT SWITCHING INSTANTS FOR EACH MODE OF OPERATION

Current	Mode I	Mode II	Mode III	Mode IV
$i_1(t_0)$	$i_2'(t_0) - I_o'$	$i_2'(t_0) - I_o'$	$i_2'(t_0) - I_o'$	$i_2'(t_0) - I_o'$
$i_1(t_1)$	$i_2'(t_1) - I_o'$	$i_2'(t_1) - I_o'$	$i_2'(t_1) - I_o'$	$i_2'(t_1) - I_o'$
$i_1(t_2)$	$i_2'(t_2) - I_o'$	$i_2'(t_2) + I_o'$	$i_2'(t_2) - I_o'$	$i_2'(t_2) - I_o'$
$i_1(t_3)$	$i_2'(t_3) + I_o'$	$i_2'(t_3) + I_o'$	$i_2'(t_3) + I_o'$	$i_2'(t_3) - I_o'$

TABLE V
DEVICE TURNING-ON AT EACH SWITCHING INSTANCE FOR EACH MODE OF OPERATION

Time instant	Mode I	Mode II	Mode III	Mode IV
t_0	S_1	S_1	S_1	S_1
t_1	Q_1	S_4	Q_1	Q_3
t_2	S_4	Q_4	Q_4	Q_1
t_3	Q_4	Q_2	S_4	S_4
t_4	S_2	S_2	S_2	S_2
t_5	Q_2	S_3	Q_2	Q_4
t_6	S_3	Q_3	Q_3	Q_2
t_7	Q_3	Q_1	S_3	S_3

The boundaries of each mode of operation can be found with respect to the power and voltage of the HV and LV battery ports i.e., V_{HV}, V_{LV}, P_2 and P_3. To calculate P_2 (expression (8)), the equivalent inductance between ports 1 and 2 i.e., $L = L_1 + L_2'$, needs to be determined. An upper limit for the leakage inductances L_1 and L_2' can be calculated from the power flow equation of the DAB operation between ports 1 and 2. More specifically, considering that the nominal power of $P_2 = 3kW$ is delivered at the HV battery when $V_{HV} = 370V$, the maximum leakage inductance between ports 1 and 2 is calculated as follows [36]

$$P_2 = \frac{V_{DC}V_{HV}}{\omega L}\phi(1 - \frac{\phi}{\pi}) \leq 3kW \implies L \leq 61.67uH \quad (10)$$

where $\phi = \frac{\pi}{2}$ has been used to achieve the maximum P_2.

As mentioned in sub-section II-B, the operation of the proposed converter does not require a specific ratio of L_1 and L_2', while also a maximum boundary for $L_1 + L_2'$ is set by (10). To simplify the analysis, $L_1 = L_2' = 6.67uH$ is assumed, which is in agreement with (10). It is shown in sub-section II-E that the proposed converter 3-DOF selection scheme can be applied for any values of L_1, L_2', as long as (10) is satisfied.

The boundaries of each mode of operation are shown in Fig. 12 for several port voltages and power levels. More specifically, Fig. 12a shows the mode boundaries for $250V \leq V_{HV} \leq 420V$ and $0.5kW \leq P_2 \leq 3kW$, while the voltage and power of port 3 are kept at nominal levels i.e., $V_{LV} = 10V$, $P_3 = 500W$. Finally, Fig. 12b shows the corresponding mode boundaries for $8V \leq V_{LV} \leq 16V$ and $100W \leq P_3 \leq 500W$ while the voltage and power level of port 2 are nominal i.e., $V_{HV} = 370V$ and $P_2 = 3kW$.

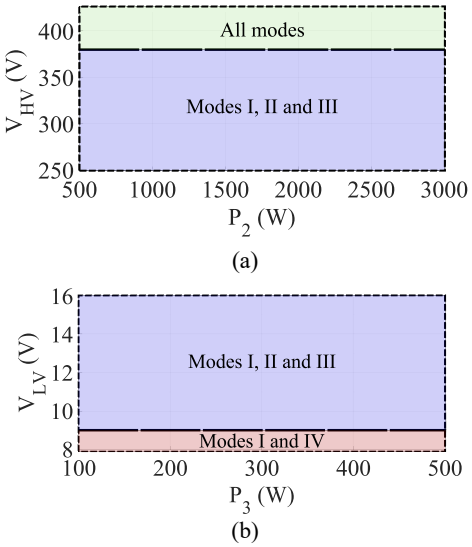

Fig. 12. Boundaries of each mode of operation for a) $250V \leq V_{HV} \leq 420V$ and $V_{LV} = 10V$, $P_3 = 500W$, b) $8V \leq V_{LV} \leq 16V$, $100W \leq P_3 \leq 500W$ and $V_{HV} = 370V$, $P_2 = 3kW$.

It can be seen from Fig. 12a that when V_{HV} is below 380V and $V_{LV} = 10V$, $P_3 = 500W$, Mode IV cannot be used to achieve the necessary P_2. In addition, Fig. 12b shows that Modes I and IV can be used in the case of $V_{HV} = 370V$, $P_2 = 3kW$ and $V_{LV} < 9V$, while Modes I, II and III can be utilized when $V_{HV} = 370V$, $P_2 = 3kW$ and $V_{LV} > 9V$.

D. ZVS analysis of the converter

It is crucial to investigate the soft-switching characteristics of the proposed converter and more specifically, ZVS turn-on capability of the switches. For this reason, polarity of the switch current during the switching instant of each semiconductor device needs to be determined [37]. To achieve ZVS during turn-on transient of a switch, the H-bridge output current needs to be flowing through the complementary switch of the corresponding phase-leg instead of the anti-parallel diode of the complementary switch. Hence, the right polarity of the H-bridge output current must be ensured. In this case, since a dead-time is required between the turn-on/off of the two complementary devices of the phase-leg, current will naturally commutate to the antiparallel diode of the device turning-on and ZVS will occur.

Since the two semiconductor switches of each H-bridge leg (half-bridge) are operated in complementary fashion, the current waveform is symmetrical for both devices. Thus, the soft-switching operation of each H-bridge leg can be determined by examining only one of the two switches. Table VI presents the requirements for ZVS operation of the semiconductor switches of port 1 and 2. More specifically, t_i, t_j, t_k and t_l indicate the turn-on instant of S_1, S_4, Q_1 and Q_4, respectively, while all currents are drain currents of the respective semiconductor switches.

TABLE VI
ZVS REQUIREMENTS OF DEVICES S_1, S_4, Q_1, Q_4

Device	ZVS condition
S_1	$i_{D,S_1}(t_i) = i_1(t_i) < 0$
S_4	$i_{D,S_4}(t_j) = i_1(t_j) < 0$
Q_1	$i_{D,Q_1}(t_k) = -i_2(t_k) < 0$
Q_4	$i_{D,Q_4}(t_l) = -i_2(t_l) < 0$

E. Selection of operation modes

Figs. 8-10 suggest that for a specific operating point of the converter i.e., designated port voltage levels and power requirements, the converter can operate with multiple combinations of ϕ, τ_1 and τ_2. Each $[\phi\ \tau_1\ \tau_2]$ set indicates converter operation in one of the five modes of Case I shown in Fig. 11. Fig. 13 shows the converter workspace for Case I at four different operating points, where variations of V_{HV}, V_{LV}, P_2 and P_3 have been considered and the corresponding converter mode of operation is presented with a specific color.

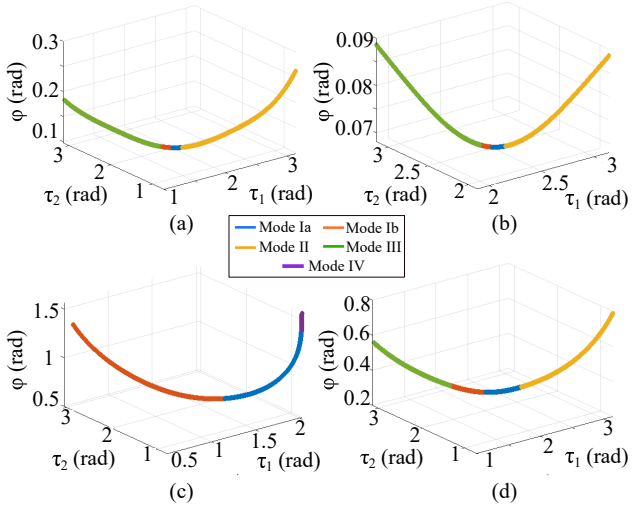

Fig. 13. Converter workspace and operating modes for a) $V_{HV} = 350V, V_{LV} = 12V, P_2 = 1kW, P_3 = 200W$, b) $V_{HV} = 400V, V_{LV} = 16V, P_2 = 1kW, P_3 = 200W$, c) $V_{HV} = 250V, V_{LV} = 8V, P_2 = 3kW, P_3 = 500W$, d) $V_{HV} = 350V, V_{LV} = 12V, P_2 = 3kW, P_3 = 500W$.

Fig. 13 indicates that operation at a given operating point can be achieved by numerous combinations of the converter 3-DOF and thus, a set of $[\phi\ \tau_1\ \tau_2]$ can be selected aiming to improve converter performance. More specifically, Tables II-IV can be used to calculate the exact values of the switching currents of all semiconductor devices for all modes of operation within the converter workspace of Case I. Comparing these values with the switching current requirements of Table VI, one can determine whether the proposed converter is operating with ZVS. Finally, a set of $[\phi\ \tau_1\ \tau_2]$ can be selected such that the converter is operating in a specific mode of operation, in which all active semiconductor devices operate with ZVS.

The selected modes of operation to achieve ZVS for all active devices of the proposed converter during simultaneous charging of the HV and LV batteries from the grid are presented in Fig. 14, where the entire range of V_{HV}, V_{LV}, P_2 and P_3 is covered. More specifically, the converter ZVS operation is investigated when the HV and LV battery voltages vary in the ranges 250∼420V and 8∼16V, respectively, while the total power delivered from the grid to the HV and LV batteries varies from $0.5kW$ to $3.5kW$. Finally, three different relationships between P_2 and P_3 are considered i.e., 1) $P_2 = P_1 - P_3, P_3 = 50W$, 2) $P_2 = P_1 - P_3, P_3 = 450W$ and 3) $P_2 = (\frac{6}{7})P_1$, $P_3 = (\frac{1}{7})P_1$.

Fig. 14 shows that all active devices of the proposed converter can operate with ZVS over wide voltage and power range. As shown in Fig. 14, all modes of operation can be used to achieve ZVS, except Mode IV. In addition, Modes Ib and III are suitable to achieve ZVS when $V_{HV} \leq 400V$, with Mode III operation preferred for low HV battery voltage levels, and Mode Ib operation dominating as V_{HV} increases. Moreover, Modes Ia and II can be used to achieve ZVS when $V_{HV} > 400V$. ZVS operation for all active semiconductor devices of the proposed converter can be achieved from low to nominal power levels, while the hard switching areas (marked with grey color) are limited. Fig. 14 shows the worst case scenario for $V_{HV} = 250V$, where hard switching of port 2 devices i.e., $Q_1 - Q_4$, occurs the most, especially when $V_{LV} > 12V$. On the other hand, Fig. 14 shows that for $V_{HV} \geq 400V$, all converter active devices can operate with ZVS over the entire range of V_{LV} and P_1.

For given converter operating conditions i.e., V_{DC}, V_{HV}, V_{LV}, P_2 and P_3, multiple combinations of $[\phi\ \tau_1\ \tau_2]$ can be selected, which correspond to the same mode of operation and result in ZVS turn-on of all active devices. For this reason, minimization of the total converter conduction loss is considered as a secondary criteria, given that ZVS is ensured for all devices. As a result, a unique solution of the converter 3-DOF can be determined for specified voltage and power levels. Fig. 15 shows the flowchart for the selection of the unique $[\phi\ \tau_1\ \tau_2]$ converter parameters for a specific operating point.

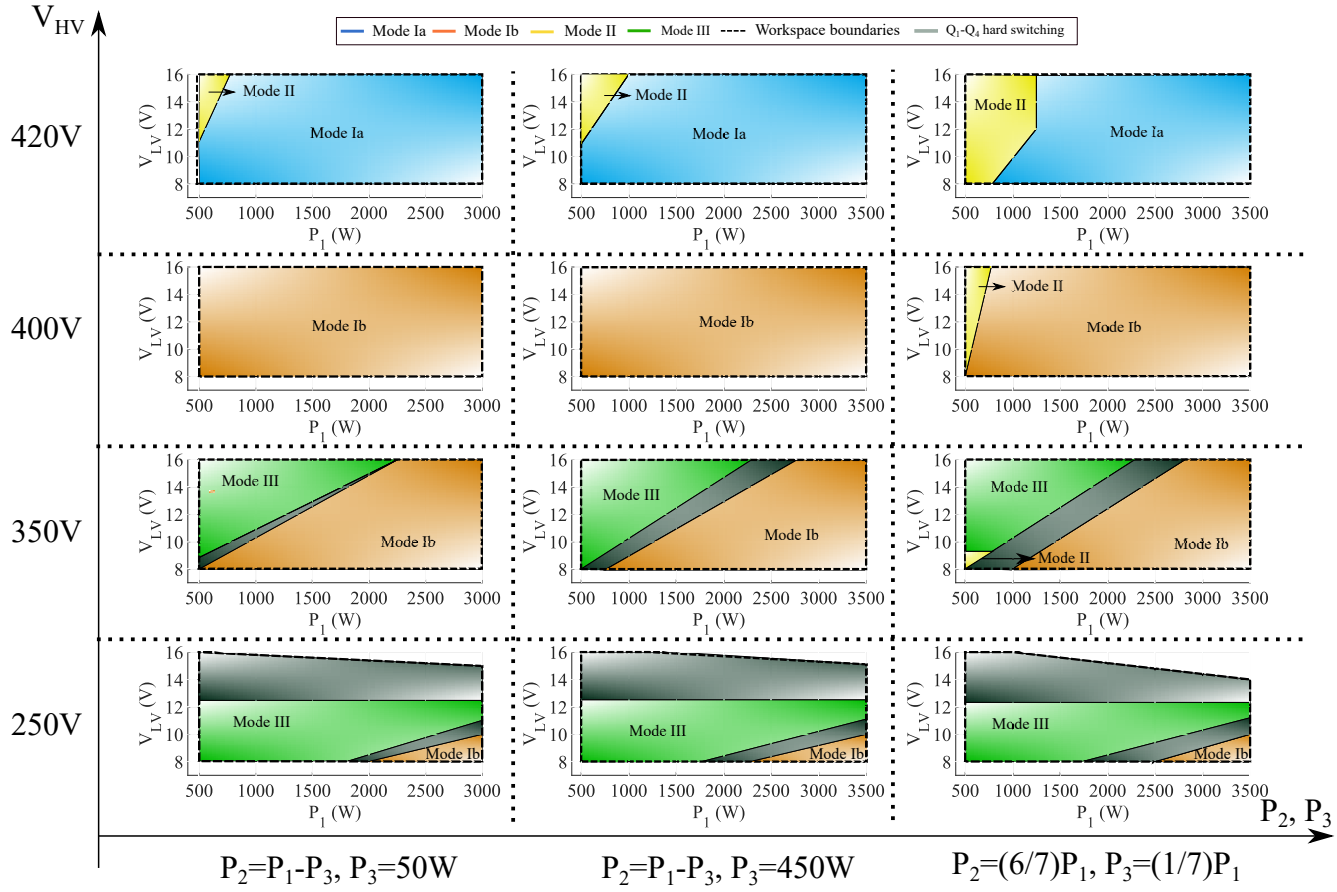

Fig. 14. ZVS range of the proposed converter for $8V \leq V_{LV} \leq 16V$, P_1 in the range $0.5kW \leq P_1 \leq 3.5kW$, $V_{HV} = 250V, 350V, 400V, 420V$ and three different relationships between P_2 and P_3 i.e., 1) $P_2 = P_1 - P_3, P_3 = 50W$, 2) $P_2 = P_1 - P_3, P_3 = 450W$ and 3) $P_2 = (\frac{6}{7})P_1$, $P_3 = (\frac{1}{7})P_1$.

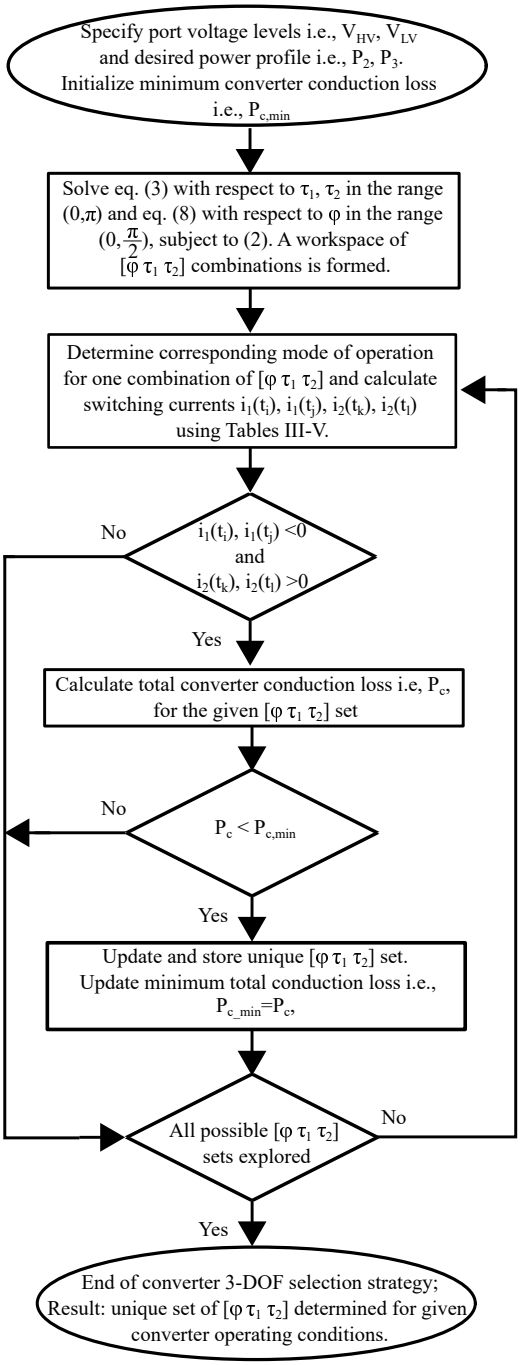

Fig. 15. Flowchart of the unique [ϕ τ_1 τ_2] parameters selection for given converter operating conditions.

As shown in Fig. 15, first, the converter operating point is identified based on the port voltage levels and power requirements i.e., V_{LV}, V_{HV}, P_2, P_3, and the converter [ϕ τ_1 τ_2] workspace is created. Then, each [ϕ τ_1 τ_2] combination is examined separately and the corresponding mode of operation of Fig. 11 is identified. The time and current expressions of Tables II- IV are utilized to calculate the switching currents of Table VI and determine whether all converter semiconductor devices are operating with ZVS for this specific combination of [ϕ τ_1 τ_2]. In case all active semiconductor devices of the proposed converter operate with ZVS, converter total conduction loss for the corresponding [ϕ τ_1 τ_2] combination i.e., P_c, is calculated and compared with the minimum converter conduction loss i.e., $P_{c,min}$, which results from the previous iterations of the [ϕ τ_1 τ_2] combinations within the converter workspace. If $P_c < P_{c,min}$, then $P_{c,min}$ is updated and set equal to P_c, while the unique [ϕ τ_1 τ_2] set is also updated. At the end of the selection scheme, a unique set of [ϕ τ_1 τ_2] parameters has been determined for a given operating point, in which all semiconductor devices operate with ZVS and conduction loss is minimum compared to the rest [ϕ τ_1 τ_2] combinations that can also achieve ZVS for all active switches.

It is clear that, to ensure wide ZVS range for all converter active switches, the proposed 3-DOF selection scheme examines each combination of [ϕ τ_1 τ_2] as a set of three and not one by one. In addition, the converter ZVS range has been presented in Fig. 14 for specific combinations of voltage and power levels with respect to the corresponding mode of operation that achieves ZVS for all active devices. However, for any converter voltage and power operating conditions, the flowchart of Fig. 15 can still be utilized to determine the suitable mode of operation that achieves ZVS for the given operating point, as long as the required V_{HV}, V_{LV}, P_2 and P_3 are within the specifications of the proposed integrated charger. Finally, it is evident from Fig. 15 that the proposed converter 3-DOF selection strategy does not set any requirement for the leakage inductances L_1 and L_2'. As a result, the flowchart of Fig. 15 can be used for any values of L_1 and L_2', as long as they satisfy (10). Consequently, for given L_1 and L_2', the corresponding converter [ϕ τ_1 τ_2] workspace is created and the unique combination of [ϕ τ_1 τ_2] is extracted, based on the converter operating conditions.

F. Constant Current and Constant Voltage charging

The proposed integrated charger operates with the constant-current (CC) and constant-voltage (CV) charging scheme [38]. The architecture of the CC/CV charging scheme is similar for both the HV and the LV batteries and is described below.

To determine the CC and CV operating range of the HV and LV batteries, $I_{HV,CC}$, $I_{LV,CC}$, $V_{HV,crit}$ and $V_{LV,crit}$ parameters are set in advance. More specifically, $V_{HV,crit}$ is the critical voltage at which charging of the HV battery changes from CC to CV mode. Moreover, $V_{HV,crit}$ is set at 370V and hence, the HV battery is in CC charging mode when V_{HV} is in the range 250V-370V, while CV charging mode occurs when V_{HV} exceeds 370V. The nominal $P_2 = 3kW$ power is delivered at the HV battery at $V_{HV} = 370V$ and the CC charging mode current is calculated $I_{HV,CC} = 8.1A$. During CC charging mode, the HV battery is charged at 8.1A, while in the CV charging mode the charging current of the HV battery is continuously decreasing with the increase of V_{HV} and is gradually reaching zero when the HV battery is fully charged. The CC and CV ranges of the LV batteries are determined similarly to the HV batteries and more specifically, $V_{LV,crit} = 10V$ and $I_{LV,CC} = 50A$. All parameters of the CC/CV charging are presented in Table VII, where the x subscript refers to either the HV or LV batteries i.e., $x = HV, LV$.

TABLE VII
CONSTANT-CURRENT (CC) AND CONSTANT-VOLTAGE (CV) CHARGING PARAMETERS FOR THE HV AND LV BATTERIES

Parameters	Symbol ($x = HV, LV$)	HV battery	LV battery
CC mode operating range	-	250V-370V	8V-10V
CV mode operating range	-	370V-420V	10V-16V
CC/CV mode transition voltage	$V_{x,crit}$	370V	10V
CC mode charging current	$I_{x,CC}$	8.1A	50A

The unique combinations of the converter 3-DOF i.e., ϕ, τ_1 and τ_2 are calculated in advance for specific operating points according to the flowchart of Fig. 15, stored in look-up tables and identified based on the converter operating conditions i.e., V_{HV}, V_{LV}, P_2 and P_3. In addition, linear interpolation is used to increase the accuracy between ϕ, τ_1 and τ_2 stored in the look-up tables. Once the unique combination of $[\phi\ \tau_1\ \tau_2]$ has been identified, the appropriate PWM signals are generated to drive the converter $S_1 - S_4$ and $Q_1 - Q_4$ devices. Fig. 16 shows the schematic diagram of the CC/CV charging scheme utilizing lookup tables.

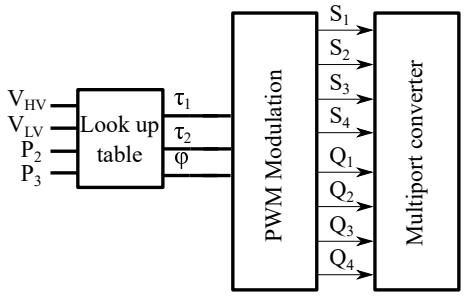

Fig. 16. Constant-current and constant-voltage charging scheme of the proposed integrated charger using lookup tables.

III. SIMULATION RESULTS

The converter is simulated using PLECS software for simultaneous HV and LV battery charging operation with the CC/CV charging scheme, using all ideal components and the simulation parameters are presented in Table VIII.

TABLE VIII
CONVERTER PLECS SIMULATION PARAMETERS

Description	Port 1	Port 2	Port 3
Voltage level (V)	400	250-420	8-16
Nominal power level (kW)	3.5	3	0.5
Leakage inductance (μH) (primary referred)	6.67	6.67	6.67
Transformer winding turns	20	20	1
Switching frequency (kHz)		100	

Fig. 17 shows the voltage and current waveforms of the HV and LV battery, as well as the converter 3-DOF, when both batteries are in the CC charging region. For simulation purposes, the capacity of each battery is set small enough, such that the charging interval of Fig. 17 lasts approximately $20ms$. During this time, V_{HV} and V_{LV} start from 360V and 9V, respectively, which correspond to the CC charging region of each battery. As a result, both batteries are charged with constant current i.e., $I_{HV,CC} = 8.1A$ and $I_{LV,CC} = 50A$, while V_{HV} and V_{LV} increase continuously.

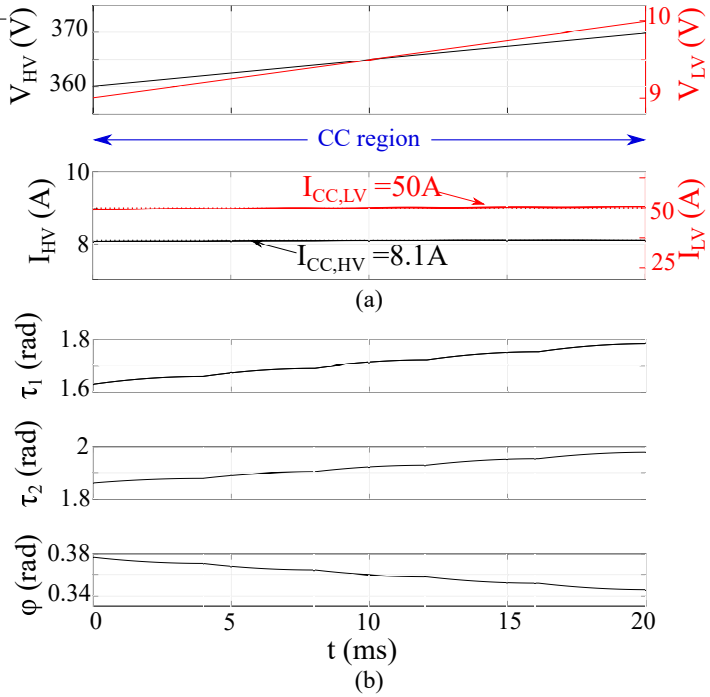

Fig. 17. a) Voltage and current waveforms of the HV and LV batteries and b) converter 3-DOF during CC charging of the HV and LV batteries.

It is evident from Fig. 17 that the currents flowing to the HV and LV batteries are $I_{HV} = 8.1A$ and $I_{LV} = 50A$ during the entire CC charging period, while the error is smaller than 2% in both cases. In addition, V_{HV} and V_{LV} increase up to $370V$ and $10V$, respectively, while the converter 3-DOF i.e., ϕ, τ_1 and τ_2 are continuously adjusted such that constant current is maintained at each battery. More specifically, depending on the levels of V_{HV}, V_{LV}, P_2 and P_3, a unique combination of $[\phi\ \tau_1\ \tau_2]$ is identified from the lookup tables and utilized for each operating point. As a result, the converter is working at the pre-defined operating point at which all active semiconductor devices operate with ZVS.

The proposed converter is operating in Mode Ib during the entire CC charging period of Fig. 17, as indicated by the converter 3-DOF. This is in line with Fig. 14, which suggests that Mode Ib is most suitable to achieve ZVS for all active switches when high P_2, P_3 are required and $V_{HV} > 350V$. Fig. 18 shows the transformer voltage and current waveforms close to nominal power operation during the CC charging period of Fig. 17 i.e., $V_{HV} = 370V$, $V_{LV} = 10V$, $P_2 = 3kW$ and $P_3 = 500W$.

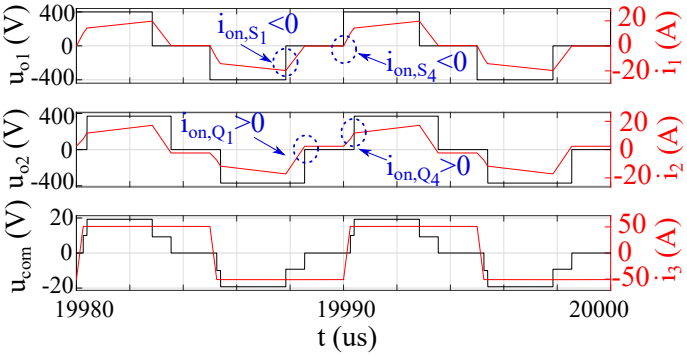

Fig. 18. Transformer voltage and current waveforms for nominal power operation in Mode Ib with $V_{DC} = 400V$, $V_{HV} = 370V$, $V_{LV} = 10V$, $P_2 = 3kW$ and $P_3 = 500W$.

As shown in Fig. 18, the transformer voltage and current waveforms indicate that the converter is operating in Mode Ib for nominal voltage and power levels. In addition, the device turn-on currents are reflected through the corresponding transformer winding currents i.e., i_1 and i_2, and according to the ZVS requirements of Table VI, all active devices of the proposed converter operate with ZVS for the nominal operating point of $V_{HV} = 370V$, $V_{LV} = 10V$, $P_2 = 3kW$ and $P_3 = 500W$.

To evaluate the performance of the proposed converter during transition between two different modes of operation, the CV charging region of the HV and LV batteries is examined. More specifically, according to the CC/CV charging scheme, the voltage across the HV and LV batteries is set at $V_{HV} = 420V$, $V_{LV} = 16V$, respectively, while I_{HV}, I_{LV} are continuously decreasing, along with the power delivered to the HV and LV batteries. Fig. 19a shows the currents flowing to the HV and LV batteries i.e., I_{HV}, I_{LV}, while the transformer voltage and current waveforms during the entire period are shown in Fig. 19b, along with the converter 3-DOF (Fig. 19c). In addition, Fig. 20 shows the transformer voltage and current waveforms for two different time intervals of the CV charging period of Fig. 19b. More specifically, the transformer voltage and current waveforms are examined at $t = 10ms$ and $t = 49ms$, which correspond to converter operation in Mode Ia and Mode II, respectively.

Fig. 19a shows that during CV charging of the HV and LV batteries, I_{HV}, I_{LV} are significantly lower compared to the CC charging of Fig. 17 and gradually reaching zero. It is evident from Fig. 19b that the transformer winding currents are also decreasing, until the converter transits from Mode Ia to Mode II, where i_1 and i_2 start to increase, while i_3 continues to decrease. The reason for this is that the converter 3-DOF are continuously adjusted based on V_{HV}, V_{LV}, P_2 and P_3, such that ZVS is achieved for all devices. As a result, when ZVS cannot be achieved for a given operating point with Mode Ia operation, the converter transits to Mode II, where ZVS is possible. It is evident from Fig. 19b that Mode II operation results in higher switching currents compared to Mode Ia, however, ZVS operation is achieved for all converter devices.

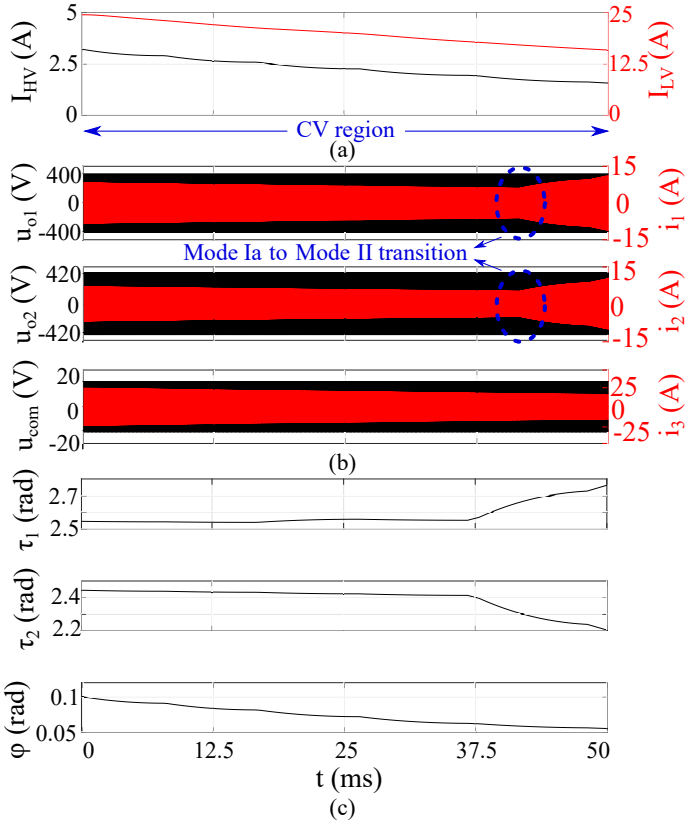

Fig. 19. a) Current waveforms of the HV and LV batteries, b) transformer voltage and current waveforms and c) converter 3-DOF during CV charging of the HV and LV batteries.

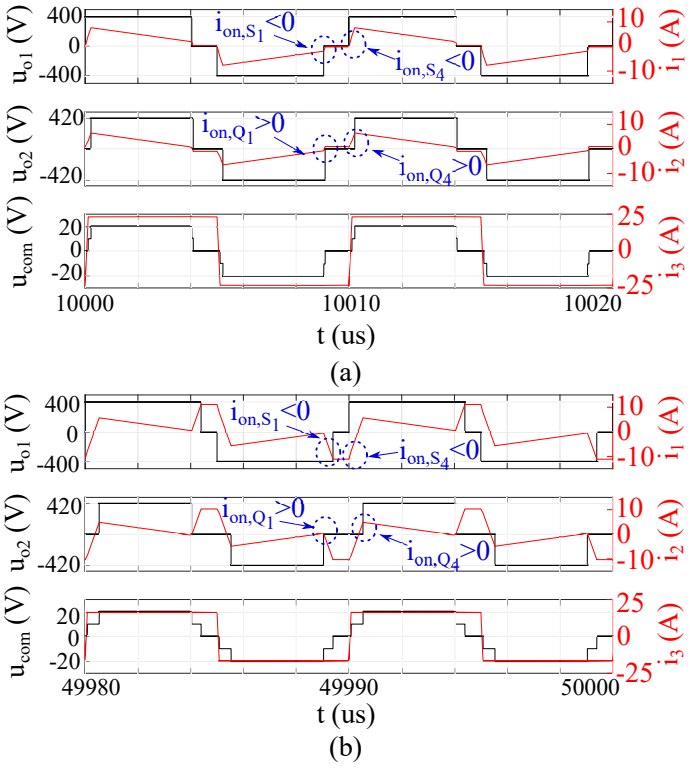

Fig. 20. Transformer voltage and current waveforms during CV charging of the HV and LV batteries and converter operation in a) Mode Ia, b) Mode II.

Finally, Fig. 20 shows the transformer voltage and current waveforms during the CV charging period, where it is evident that the converter operates initially in Mode Ia and ultimately in Mode II. By examining the polarity of the transformer primary and secondary winding current during the device turn-on instances, it is again verified that all converter devices operate with ZVS for both Mode Ia and Mode II operation. The latter is in accordance with Fig.14, which suggests that Mode Ia and Mode II are used to achieve ZVS when $V_{HV} = 420V, V_{LV} = 16V$, while also the converter transits from Mode Ia to Mode II when P_2 and P_3 decrease.

IV. Experimental Results

A laboratory prototype of the proposed converter is developed and tested. The converter is operated at 100kHz and can deliver 3kW and 500W simultaneously to the HV and LV batteries, respectively. SCT015W120G3-4AG SiC MOSFET devices are used for the active switches for ports 1 and 2, while IPP016N08NF2S Si MOSFETs are utilized for port 3. Although Si diodes can be selected for port 3, active switches are preferred as synchronous rectification scheme can be adopted to increase the converter efficiency. A control board is implemented based on the LAUNCHXL-F28379D development kit with the TMS320F28379D microprocessor and is used to generate the PWM signals based on the desired ϕ, τ_1 and τ_2 control parameters.

The three-winding transformer is implemented using a set of N87 E71 ferrite cores, while all three windings are winded around the middle leg of the core. Primary and secondary windings consist of 20 turns of Litz wire, while tertiary winding utilizes 1 turn of copper foil. Characterization of the three-winding transformer is performed according to [39] and is verified by ANSYS simulations. The output filter inductor of port 3 i.e., L_f, is chosen 150uH to eliminate the ripple in the output current I_{LV}, as suggested by the analysis of Section II. The specifications of the converter prototype are presented in Table IX.

TABLE IX
Key Parameters Of The Proposed Integrated Charger

Parameters	Symbol	Values
HV-bridge switches	$S_1 - S_4,\ Q_1 - Q_4$	1.2kV, 15.5mΩ
LV-bridge switches	$D_1 - D_4$	80V, 0.88V
Primary bridge DC capacitance	C_1	13.2uF/630V
Secondary bridge DC capacitance	C_2	2uF/630V
Output inductor	L_f	150uH
Magnetizing inductance	L_m	4.5mH
Primary leakage inductance	L_1	7.2uH
Secondary leakage inductance (primary referred)	L_2'	1.2uH
Tertiary leakage inductance (primary referred)	L_3'	8uH
Transformer turns ratio	$n_1 : n_2 : n_3$	20:20:1
Switching frequency	f_s	100kHz

Table IX shows the value of the tertiary winding leakage inductance with respect to primary i.e., $L_3' = 8uH$, which is in the same range with $L_1 = 7.2uH$ and $L_2' = 1.2uH$. However, $L_3' = 8uH$ has small impact on the operation of the proposed converter and results in less than 5% error on the output voltage of port 3 i.e., V_{LV}. As a result, the assumption of neglecting L_3' throughout the analysis of Section II is valid. In addition, according to Table IX, the experimental prototype utilizes $L_1 \neq L_2'$, while the analysis and simulation of the proposed converter in Sections II and III have been presented for $L_1 = L_2'$. However, the converter experimental results verify that $L_1 \neq L_2'$ does not impact the operation of the proposed converter. The reason for this is that for a given operating point, the converter 3-DOF i.e., ϕ, τ_1 and τ_2, are calculated according to expression (3) and ultimately selected using the flowchart of Fig. 15, which are valid for any combination of L_1 and L_2' that satisfy (10).

Two power supplies with bidirectional power flow capability are connected at ports 1 and 2 to set V_{DC} and V_{HV}. Port 1 voltage i.e., V_{DC}, is fixed at 400V for all experiments. Finally, the experimental setup of the proposed integrated charger is shown in Fig. 21.

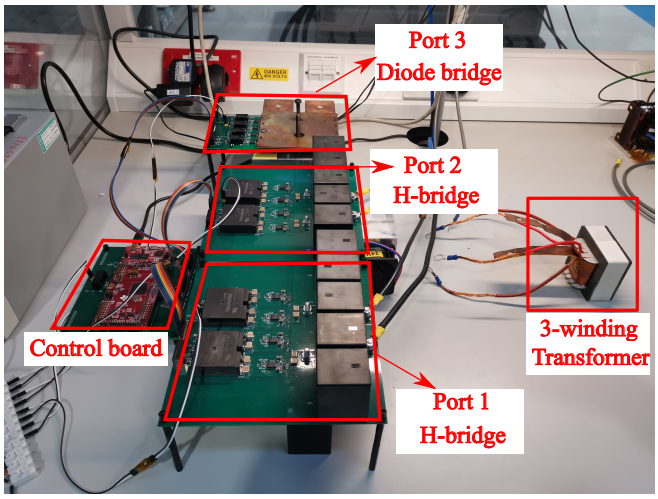

Fig. 21. Experimental setup of the proposed integrated charger.

Several tests are performed and the proposed converter is operated for simultaneous HV and LV battery charging to verify the theoretical analysis (Figs. 22-31). Then, the converter is also tested as traditional PSFB converter to charge the LV battery from the HV battery (Figs. 32-33). Case I operation has only been considered for all converter experiments and the values of ϕ, τ_1 and τ_2 are given in rad for each experiment.

Experiment 1: First, the converter is tested to generate the minimum specified voltage of 8V at the LV port i.e., $V_{LV} = 8V$, while the HV battery port is operating close to the CC/CV mode transition and $P_2 = 2.9kW$, $V_{HV} = 360V$ (Table VII). In addition, the load of the LV port is adjusted such that the output current i.e., I_{LV}, is close to 50A, according to Table VII. The converter operates with $\phi = 0.02$, $\tau_1 = 2.8$ and $\tau_2 = 2.9$ and the corresponding waveforms are shown in Fig. 22.

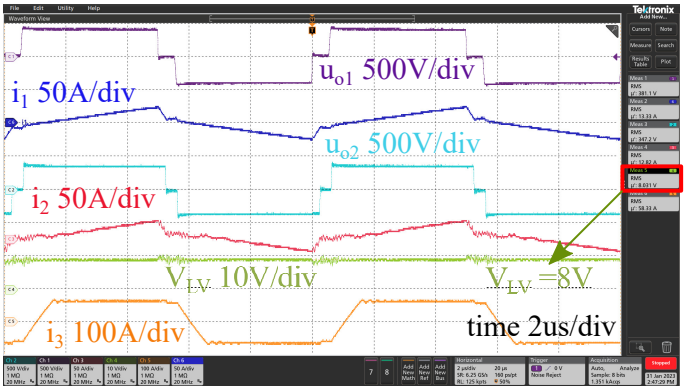

Fig. 22. Experimental converter voltage and current waveforms for simultaneous HV and LV battery charging operation and $V_{DC} = 400V, V_{HV} = 360V, V_{LV} = 8V, \tau_1 = 2.8, \tau_2 = 2.9$ and $\phi = 0.02$; $P_2 = 2.9kW$ and $P_3 = 460W$.

It is evident from Fig. 22 that the converter can produce 8V at the LV battery port, while at the same time 2.9kW are delivered from the grid to the HV battery port. Fig. 22 also confirms that the transformer primary winding current results from the secondary and tertiary winding currents i.e., $i_1 = i_2' + i_3'$. Moreover, the tertiary winding current has a trapezoidal shape due to the tertiary winding leakage inductance i.e., L_3. As a result, when i_3 is changing polarity from I_o to $-I_o$ and vice versa, commutation effect takes place in the diode bridge of port 3 and i_3 deviates from the ideal square waveform.

Experiment 2: Similarly to Experiment 1, the converter is tested to generate the maximum specified voltage of $V_{LV} = 16V$, while V_{HV} is set at 380V. The power requirements for the HV and LV batteries are set at $P_2 = 1.8kW$ and $P_3 = 110W$. The latter is in accordance with Table VII, which suggests that when battery voltage is in the CV region, the power delivered to the battery is decreasing with the increase of voltage. Hence, P_2 and P_3 requirements are decreased compared to the values of Experiment 1. The converter operates with $\phi = 0.01$, $\tau_1 = 3$ and $\tau_2 = 3.1$ and the resulting waveforms are shown in Fig. 23.

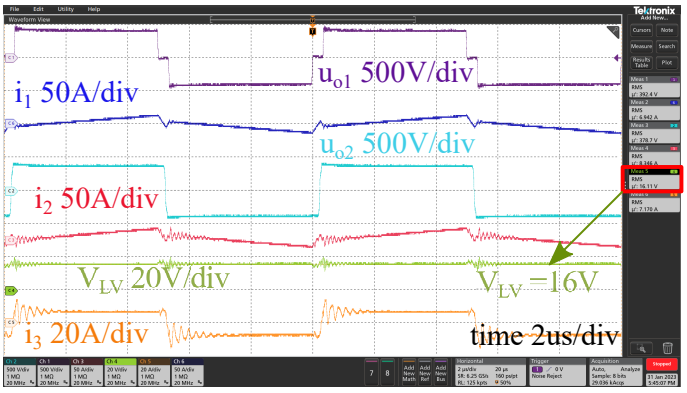

Fig. 23. Experimental converter voltage and current waveforms for simultaneous HV and LV battery charging operation and $V_{DC} = 400V, V_{HV} = 380V, V_{LV} = 16V, \tau_1 = 3, \tau_2 = 3.1$ and $\phi = 0.01$; $P_2 = 1.8kW$ and $P_3 = 110W$.

As shown in Fig. 23, the converter is capable of generating 16V at the LV port, while 1.8kW and 110W are delivered to the HV and LV battery ports, respectively. In addition, τ_1 and τ_2 are increased compared to Fig. 22 and almost the whole duty cycle is utilized to generate the maximum 16V. Finally, it is evident from Fig. 23 that i_3 is close to the ideal square waveform and the commutation effect is weak. The reason for this is that due to the low power requirement of port 3 i.e., $P_3 = 110W$, the amplitude of i_3 is decreased and commutation time is significantly reduced.

Experiment 3: In this experiment, the converter independent power flow operation is evaluated according to the modulation scheme proposed in sub-section II-B. More specifically, V_{HV} is set at 380V, $\tau_1 = 2.2$, $\tau_2 = 2.9$ are selected such that $V_{LV} = 10V$, while V_{DC} remains fixed at 400V. According to the proposed modulation scheme, when the converter operates as in Case I (Fig. 7), V_{LV} is independent of ϕ, which can be utilized to control the power at the HV battery port. Fig. 24 shows the corresponding converter waveforms for the above operating conditions and two different values of ϕ.

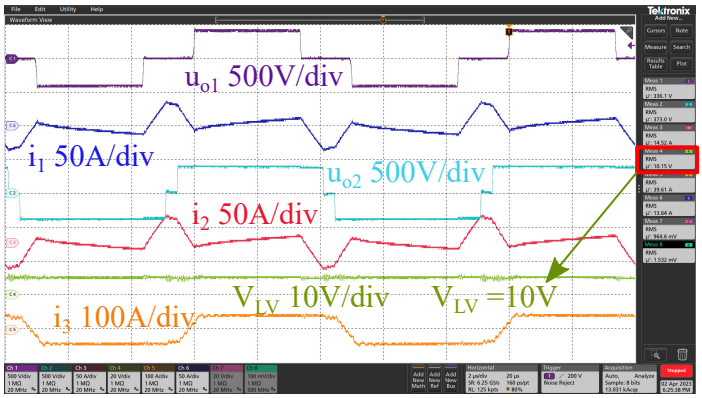

(a)

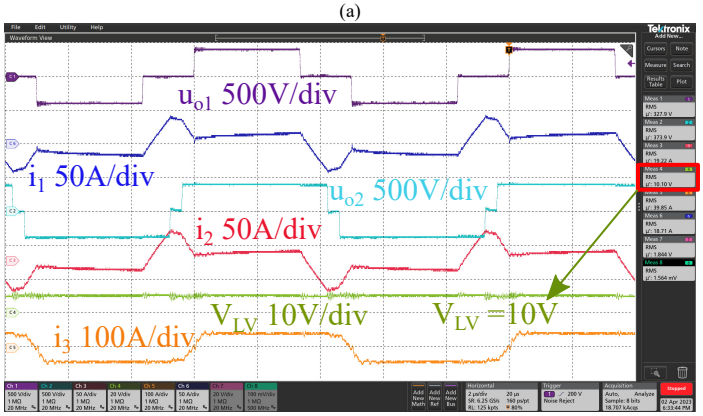

(b)

Fig. 24. Experimental converter voltage and current waveforms for simultaneous HV and LV battery charging operation, $V_{DC} = 400V, V_{HV} = 380V, V_{LV} = 10V, P_3 = 400W, \tau_1 = 2.2, \tau_2 = 2.9$, a) $\phi = 0.1$, $P_2 = 1.2kW$ and b) $P_2 = 3kW$, $\phi = 0.2$.

It is evident from Fig. 24 that although ϕ is increased from 0.1 to 0.2, the output voltage at the LV battery port remains constant at 10V, since τ_1 and τ_2 are kept constant and the converter requirements for Case I operation are satisfied. In addition, when ϕ is increased from 0.1 to 0.2, power flow at the HV battery port is also increased from $P_2 = 1.2kW$ to $P_2 = 3kW$, while power at the LV battery port remains constant at 400W. As a result, the proposed modulation scheme

is validated and τ_1, τ_2 can be selected to produce the desired V_{LV} at port 3, while ϕ can be independently selected to adjust the power flowing to the HV battery port.

Experiment 4: The proposed converter is first tested for simultaneous charging operation for power close to nominal levels. According to Table VII, during simultaneous charging operation, maximum power flow occurs when both batteries are in the transition between CC and CV charging mode. Hence, V_{HV} and V_{LV} are selected close to 370V and 10V, respectively. In addition, $\tau_1 = 2.5$ and $\tau_2 = 2.9$, so that the desired voltage of 10V is produced at the LV battery port, while also the LV port load is adjusted so that output current is close to 50A i.e., $I_{LV} = 50A$. Finally, ϕ is selected 0.15 to achieve the nominal power transfer at the HV battery port i.e., $P_2 = 3kW$. The corresponding converter waveforms are presented in Fig. 25.

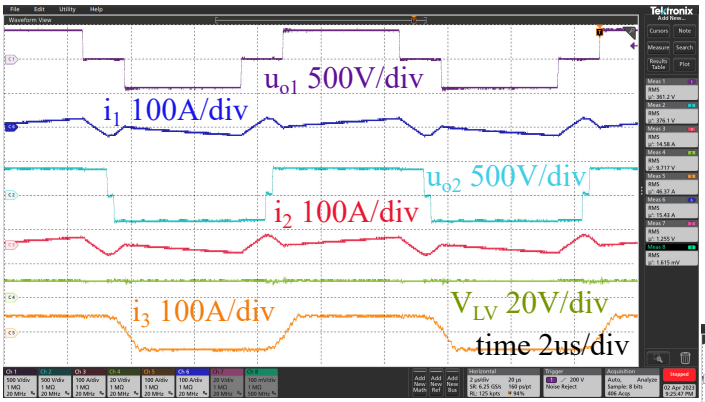

Fig. 25. Experimental converter voltage and current waveforms for rated simultaneous HV and LV battery charging operation and $V_{DC} = 400V, V_{HV} = 380V, V_{LV} = 10V, \tau_1 = 2.5, \tau_2 = 2.9$ and $\phi = 0.15$; $P_2 = 3kW$ and $P_3 = 450W$.

It can be seen from Fig. 25 that, with the above operating parameters, the converter can achieve power flow close to nominal levels i.e., $P_2 = 3kW$, $P_3 = 450W$, for the HV and LV battery ports, respectively. In addition, the converter 3-DOF correspond to Mode III operation, which agrees with the respective voltage and current waveforms. Finally, commutation effect in the diode bridge of port 3 is again present when i_3 is changing polarity, due to the fact that the amplitude of i_3 is significantly high and commutation time is increased.

The proposed converter is then tested for the case where nominal power is transferred to the HV battery port, while the LV battery is considered fully charged and hence, $P_3 = 0W$. As suggested by the CC/CV charging scheme of Table VII, the nominal power of $3kW$ is delivered to the HV battery when $V_{HV} = 370V$, while $P_3 = 0W$ corresponds to $V_{LV} = 16V$ (fully charged LV battery). In this case, the converter operates with $\tau_1 = 2.5$, $\tau_2 = 2.9$ and $\phi = 0.1$ and the results are shown in Fig. 26.

It is evident from Fig. 26 that $V_{LV} = 16V$ at port 3, while at the same time the tertiary winding current is zero i.e., $i_3 = 0A$, which confirms that there is no power flow at port 3 i.e., $P_3 = 0W$. In addition, nominal power $P_2 = 3kW$ flows from the grid to the HV battery port.

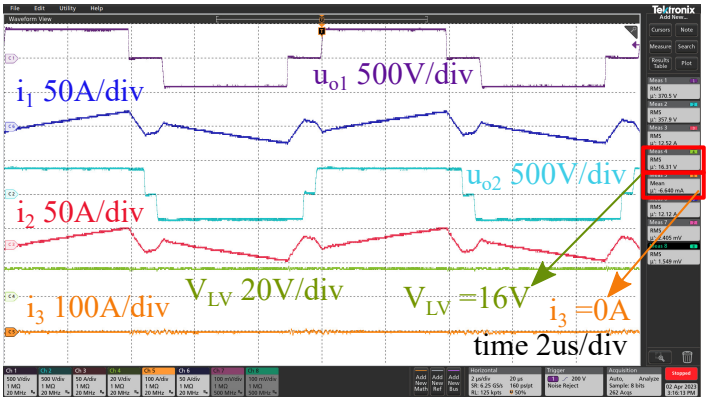

Fig. 26. Experimental converter voltage and current waveforms for simultaneous HV and LV battery charging operation and $V_{DC} = 400V$, $V_{HV} = 370V, V_{LV} = 16V, P_2 = 3kW, P_3 = 0W, \tau_1 = 2.5, \tau_2 = 2.9, \phi = 0.1$.

The converter is also tested for the case where the HV battery is fully charged i.e., $V_{HV} = 420V$ and P_2 is close to zero, while the LV battery voltage is at the lower limit i.e., $V_{LV} = 8V$. According to the CC/CV charging scheme (Table VII), the LV battery is charged in the CC region with $I_{LV} = 50A$ and for this reason, the converter 3-DOF are selected as $\tau_1 = 2.8$, $\tau_2 = 2.5$ and $\phi = 0.02$ to achieve $P_3 = 400W$. The corresponding converter voltage and current waveforms are shown in Fig. 27.

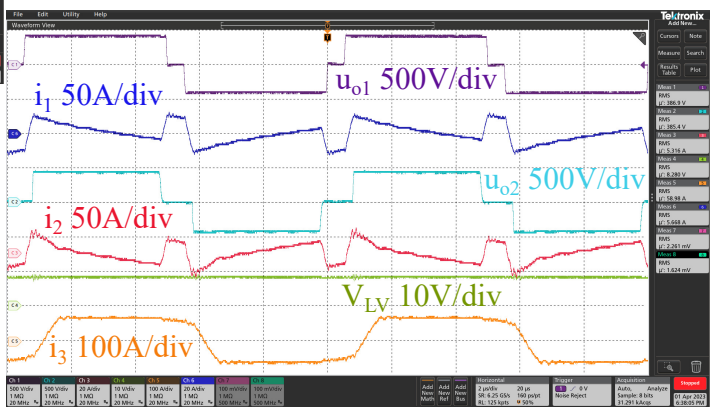

Fig. 27. Experimental converter voltage and current waveforms for simultaneous HV and LV battery charging operation and $V_{DC} = 400V$, a) $V_{HV} = 420V, V_{LV} = 8V, P_2 = 0W, P_3 = 400W, \tau_1 = 2.8, \tau_2 = 2.5, \phi = 0.02$.

It can be seen from Fig. 27 that the converter waveforms correspond to Mode II operation when $V_{HV} = 420V$. In addition, i_3 has a trapezoidal shape due to the commutation effect at port 3, which however does not impact the converter operation, since the required voltage and current are generated at port 3.

Experiment 5: In this experiment, the ZVS capability of the converter semiconductor devices is evaluated. To begin with, both low and nominal port 2 power requirements are considered, while port 3 power is set close to nominal levels. The converter ZVS capability is first examined for low port 2 power operation and more specifically, for the operating point of $V_{DC} = 400V$, $V_{HV} = 370V$, $V_{LV} = 10V$, $P_2 = 1.2kW$, $P_3 = 430W$, $\phi = 0.1$, $\tau_1 = 2.2$ and $\tau_2 = 2.9$. The

drain-to-source (u_{DS}) and gate-to-source (u_{GS}) voltages of semiconductor devices S_1, S_4, Q_1 and Q_4 are shown in Fig. 28, along with the transformer primary and secondary winding currents.

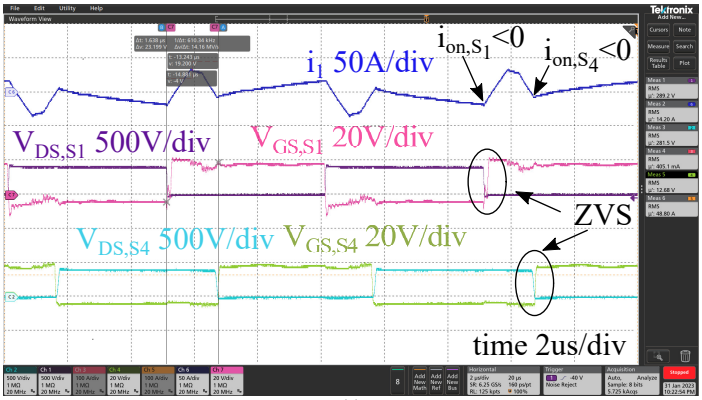

(a)

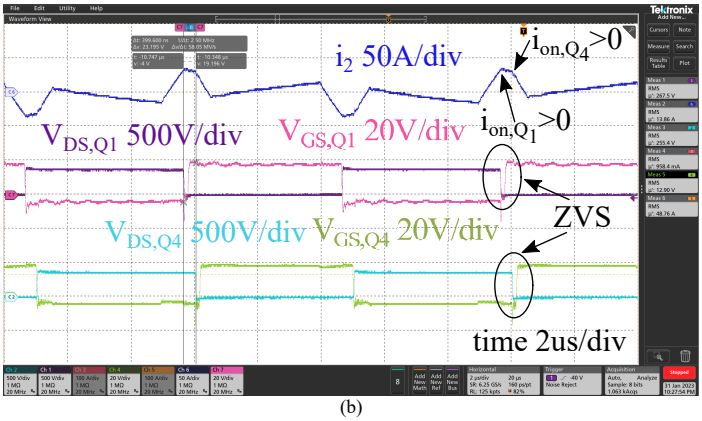

(b)

Fig. 28. Experimental voltage and current waveforms for simultaneous HV and LV battery charging operation and $V_{DC} = 400V, V_{HV} = 370V, V_{LV} = 10V, P_2 = 1.2kW, P_3 = 430W, \tau_1 = 2.2, \tau_2 = 2.9$ and $\phi = 0.1$; a) S_1, S_4 and b) Q_1, Q_4 devices.

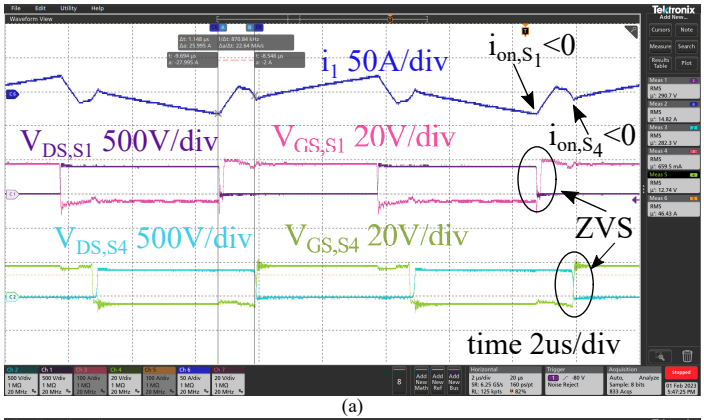

(a)

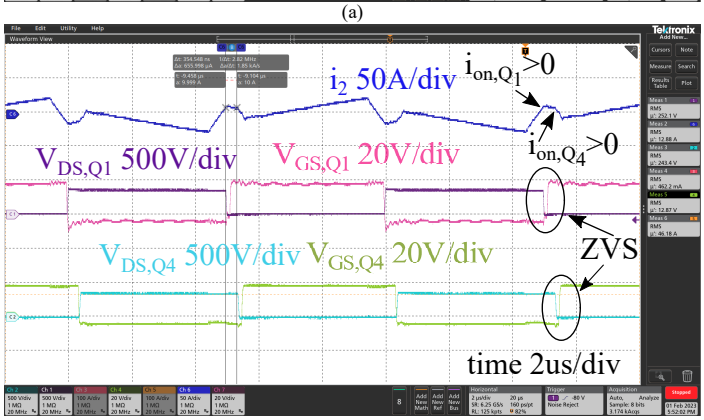

(b)

Fig. 29. Experimental voltage and current waveforms for high power simultaneous HV and LV battery charging operation and $V_{DC} = 400V, V_{HV} = 370V, V_{LV} = 10V, P_2 = 2.9kW, P_3 = 450W, \tau_1 = 2.5, \tau_2 = 2.9$ and $\phi = 0.15$; a) S_1, S_4 and b) Q_1, Q_4 devices.

Fig. 28 shows that all semiconductor devices of the proposed converter operate with ZVS for the given operating point of low port 2 power requirement i.e., $P_2 = 1.2kW$, while $P_3 = 430W$. More specifically, when the gate-to-source voltage of one semiconductor device starts to rise, drain-to-source voltage is already close to 0, since current is flowing through the antiparallel diode of the device. Hence, ZVS is achieved. In addition, it is evident that the transformer primary winding current i.e., i_1, is negative during turn-on of S_1 and S_4, while the current of the secondary winding of the transformer i.e., i_2, is positive during turn-on of Q_1 and Q_4, as shown by the cursors in Fig. 28. This is in line with the ZVS analysis of sub-section II-D and verifies ZVS operation for all active switches of the proposed converter.

Fig. 29 shows the semiconductor devices waveforms along with the transformer primary and secondary currents for close to nominal P_2 and P_3 power requirements, where again the ZVS operation of all switches is verified. For the operating point of Fig. 29 the converter operates close to nominal power levels with $V_{DC} = 400V$, $V_{HV} = 370V$, $V_{LV} = 10V$, $P_2 = 2.9kW$, $P_3 = 450W$, $\phi = 0.15$, $\tau_1 = 2.5$ and $\tau_2 = 2.9$.

Examining the drain-to-source and gate-to-source waveforms of the semiconductor devices in Fig. 29, as well as the transformer primary and secondary winding current polarity during switching instants, it clear that all converter semiconductor devices operate with ZVS. In the case of device S_4, a short period of overlap between the drain-to-source and gate-to-source voltages is present. However, when the drain-to-source voltage of S_4 reaches zero, gate-to-source voltage is around 3V, which is below the device turn-on threshold level and thus, ZVS is achieved. The latter is further verified by the polarity of S_4 turn-on current i.e., $i_{on,S_4} < 0$.

The converter ZVS capability is examined for two more cases and more specifically, for the operating points of Figs. 26-27. In the case of Fig. 26, the LV battery is fully charged and $P_3 = 0W$, $V_{LV} = 16V$, while nominal power is delivered to the HV battery i.e., $P_2 = 3kW$, $V_{HV} = 370V$. Similarly for Fig. 27, the HV battery is fully charged and $P_2 = 0W$, $V_{HV} = 420V$, while $P_3 = 400W$, $V_{LV} = 8V$. Figs. 30-31 show the gate-to-source and drain-to-source voltages of semiconductor devices S_1, S_4, Q_1 and Q_4 along with the transformer primary and secondary winding currents i.e., i_1 and i_2.

By examining the polarity of the primary and secondary winding currents during switching instants, as well as the u_{DS} and u_{GS} waveforms of the devices, Figs. 30-31 confirm that ZVS is achieved for devices S_1, S_4, Q_1 and Q_4. Finally, according to the analysis of sub-section II-D, due to the

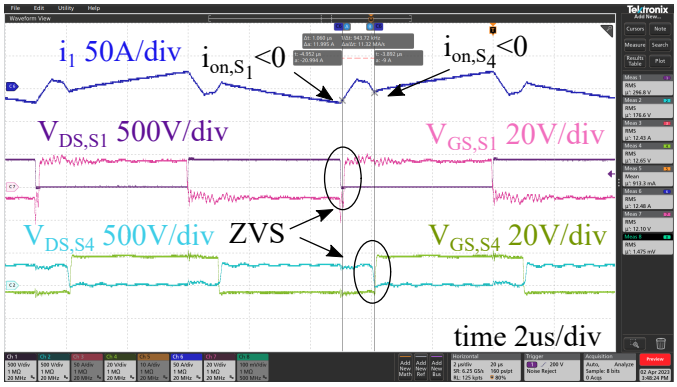

(a)

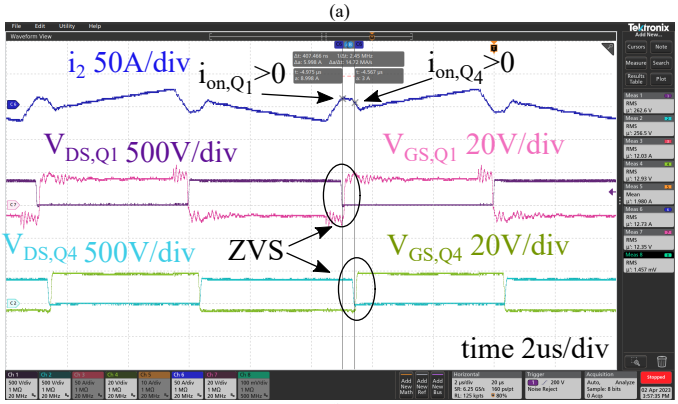

(b)

Fig. 30. Experimental converter voltage and current waveforms for simultaneous HV and LV battery charging operation and $V_{DC} = 400V$, $V_{HV} = 370V, V_{LV} = 16V, P_2 = 3kW, P_3 = 0W, \tau_1 = 2.5, \tau_2 = 2.9, \phi = 0.1$.

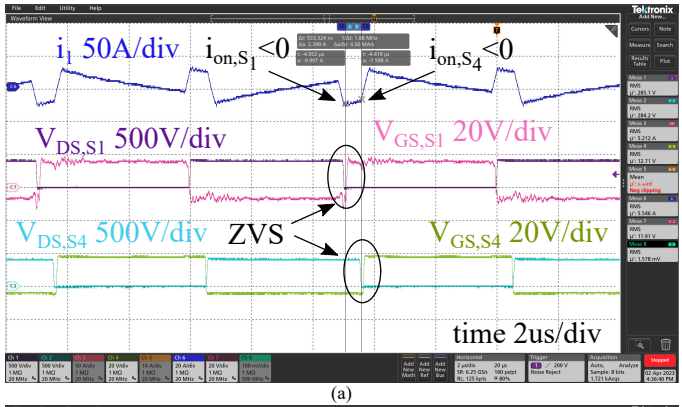

(a)

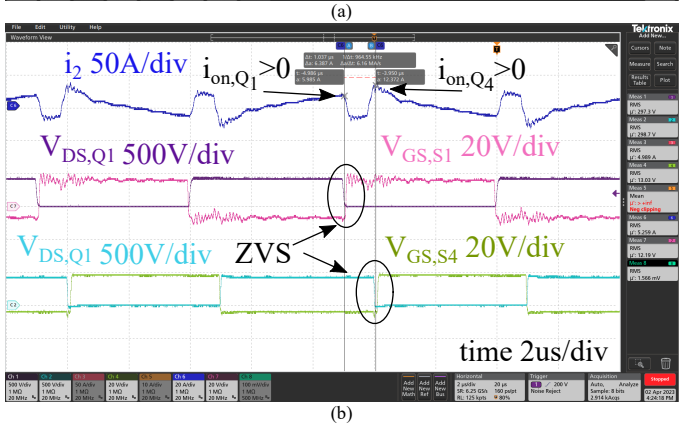

(b)

Fig. 31. Experimental converter voltage and current waveforms for simultaneous HV and LV battery charging operation and $V_{DC} = 400V$, a) $V_{HV} = 420V, V_{LV} = 8V, P_2 = 0kW, P_3 = 400W, \tau_1 = 2.8, \tau_2 = 2.5, \phi = 0.02$.

symmetric converter operation, since ZVS is achieved for a device of a specific phase-leg, ZVS is also guaranteed for the complementary device of the phase-leg. As a result, all converter active switches can operate with ZVS for the above two extreme case operating points.

Experiment 6: Finally, the converter is tested for HV to LV battery charging operation. Hence, port 1 is disconnected and power is transferred from port 2 to port 3. The converter operates as a PSFB converter with $V_{HV} = 400V$ and $\tau_2 = 2.7$, aiming to produce $V_{LV} = 10V$. In addition, the power delivered at the LV battery port is $P_3 = 480W$. Fig. 32 shows the voltage and current waveforms of the transformer secondary winding, along with the transformer tertiary winding current and the output voltage at the LV port of the converter.

Fig. 32 shows that 10V are generated at the output of the LV battery port, when the proposed converter operates as a traditional PSFB with $\tau_2 = 2.7$. It is also evident from Fig. 32 that the transformer tertiary winding current i.e., i_3, has a trapezoidal shape due to the commutation effect in the diode bridge of port 3, similarly to the simultaneous charging operation of the proposed integrated converter. More specifically, rated power is transferred to the LV battery port and I_{LV} is significantly high i.e, 50A, which results in increased commutation time. Finally, it is seen that for converter PSFB operation, the transformer secondary winding current i.e., i_2, has also a trapezoidal shape similar to i_3, scaled down by the transformer turns ratio i.e., $i_2 = (\frac{n_3}{n_2})i_3$.

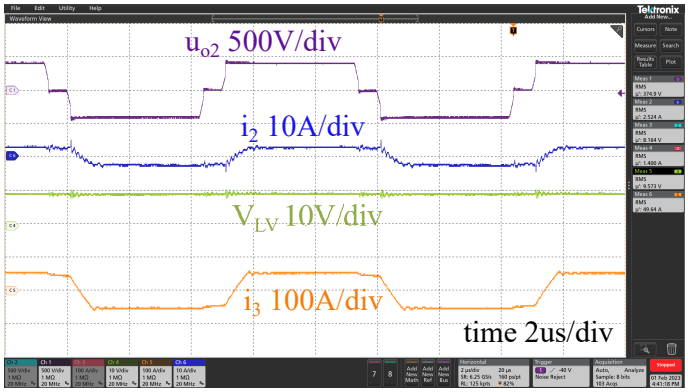

Fig. 32. Experimental PSFB converter voltage and current waveforms for HV to LV battery charging operation and $V_{HV} = 400V, \tau_2 = 2.7$, $V_{LV} = 10V$ and $P_3 = 480W$.

The converter HV to LV charging function is further investigated in Fig. 33 with respect to the primary winding of the three-winding transformer. Although port 1 is disconnected from the grid and left open during HV to LV charging function, it is still magnetically coupled to the HV and LV ports, due to the three-winding transformer. Fig. 33 shows the DC of voltage of port 1 i.e., V_{DC}, as well as the current of the primary winding of the transformer during converter PSFB operation and HV to LV charging at nominal power levels.

When the converter PSFB operation starts, voltage is induced at the primary winding of the transformer and it is

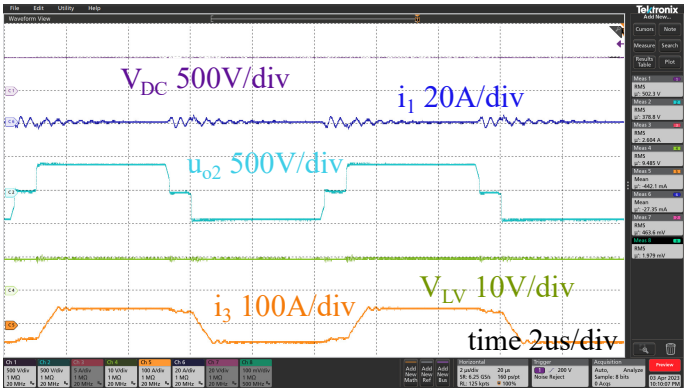

Fig. 33. Experimental PSFB converter voltage and current waveforms for HV to LV battery charging operation and $V_{HV} = 400V, \tau_2 = 2.7, V_{LV} = 10V$ and $P_3 = 480W$.

rectified through the body diodes of the semiconductor devices of port 1. As a result, current flows in port 1 and the DC link capacitor of port 1 is charged. When V_{DC} exceeds the induced voltage at the primary winding, current stops flowing in port 1. As a result, V_{DC} remains constant and the converter operates as PSFB in steady state (Fig. 33).

The active switches of port 1 are not modulated during PSFB operation, however, it is evident from Fig. 33 that a resonant current exists in the primary winding of the transformer i.e., i_1. This resonant current is the result of a high-frequency LC resonance between the device parasitic capacitance and the primary winding leakage inductance. However, the magnitude of the resonant current i_1 is low and does not impact the converter HV to LV charging operation.

V. Converter Efficiency and Loss Analysis

The efficiency of the proposed converter for simultaneous HV and LV battery charging from the grid is shown in Fig. 34 for several operating points. More specifically, in Fig. 34a, the voltage and power of the LV battery are set at nominal levels i.e., $V_{LV} = 10V$, $P_3 = 500W$, while the HV battery power varies from $500W$ to $3kW$. In Fig. 34b, the voltage and power of the HV battery are set at nominal levels i.e., $V_{HV} = 370V$, $P_2 = 3kW$, while P_3 varies from $100W$ to $500W$. Finally, the efficiency of the proposed converter is demonstrated in Fig. 34c for $1kW \leq P_2 + P_3 \leq 3.5kW$ and constant power ratio i.e., $(P_2/P_3) = 6$. For all cases, two different operations have been considered for the diode bridge of port 3 i.e., 1) operation with the device body diodes and 2) synchronous rectification modulation. The corresponding loss breakdown analyses are shown in Figs. 35a-b.

The efficiency of the proposed converter for the nominal operating point of $V_{LV} = 10V$, $P_3 = 500W$, $V_{HV} = 370V$, $P_2 = 3kW$ is 94% when diodes are utilized at port 3, while efficiency can be increased to 97% using synchronous rectification modulation. Results show that in the first case, when the body diodes of the devices of port 3 are used, conduction loss accounts for 63% of the converter total loss, while also conduction loss of port 3 diodes reaches 100W. In the case of synchronous rectification scheme, conduction loss of port 3 devices is reduced by more than 10 times, while

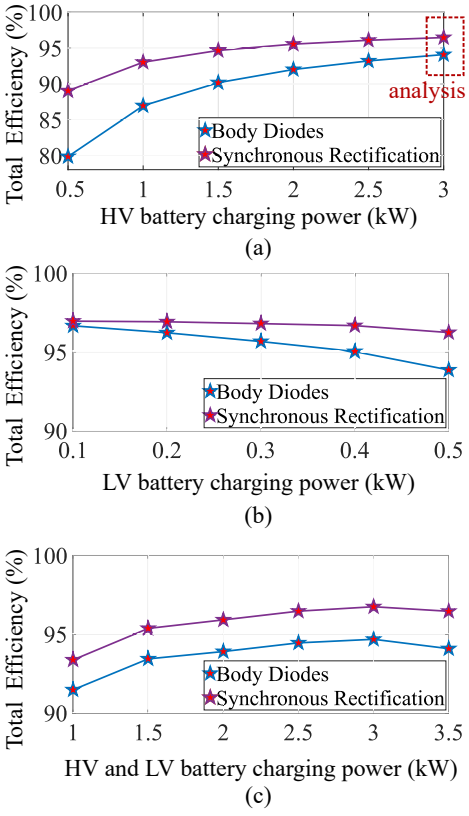

Fig. 34. Total efficiency of the proposed converter for a) $V_{LV} = 10V$, $P_3 = 500W$ and $0.5kW \leq P_2 \leq 3kW$, b) $V_{HV} = 370V$, $P_2 = 3kW$ and $0.1kW \leq P_3 \leq 0.5kW$, c) $1kW \leq P_2 + P_3 \leq 3.5kW$ and $(P_2/P_3) = 6$.

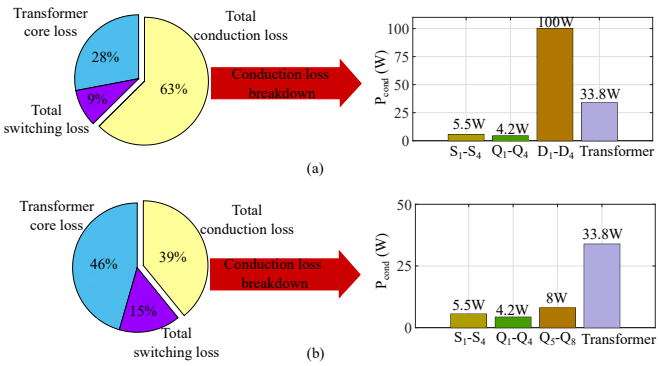

Fig. 35. Converter loss breakdown for $V_{LV} = 10V$, $P_3 = 500W$, $V_{HV} = 370V$, $P_2 = 3kW$ and a) device body diode conduction, b) synchronous rectification modulation.

the transformer core and conduction loss account for most of the loss in the converter. More specifically, to extract the transformer conduction loss for nominal power operation i.e., $P_2 = 3kW$ and $P_3 = 500W$, first, the transformer winding currents were measured when the converter operates with the proposed 3-DOF scheme of Fig. 15. Next, the transformer primary, secondary and tertiary winding resistances were measured at the operating switching frequency of $100kHz$ using the impedance analyzer and transformer conduction loss is estimated at approximately 34W. Finally, due to the ZVS operation of the active switches of ports 1 and 2, total converter

switching loss is mostly due to the device turn-off loss and accounts for 9% when body diodes are utilized at port 3, while switching loss corresponds to 15% when synchronous rectification modulation is applied at port 3.

VI. Comparison With Other Chargers

The three-winding transformer with the E71/33/32 cores used for the integrated converter is compared to the individual two-winding DAB and PSFB transformers of the conventional OBC and APM, which are based on E65/33/27 and E55/28/21 cores, respectively. The design parameters for all transformers are presented in Table X, while core selection is performed based on the calculated Area-Product (AP) of each transformer. For a fair comparison, a 3-DOF operation and an RMS current minimization scheme are adopted for both the integrated charger and the separate DAB OBC charger. More specifically, the 3-DOF of the integrated charger are selected such that the nominal power of $P_2 = 3kW$, $P_3 = 500W$ occurs, while at the same time transformer RMS current is minimum. For the DAB OBC charger, 3-DOF are selected for $P_{OBC} = 3kW$ while transformer current remains minimum.

Magnetic core loss and winding copper loss are estimated for the three-winding transformer and the individual OBC and APM transformers and the results are presented in Fig. 36. For a fair comparison, the same core material is selected for all transformers and core loss is $P_v = 280kW/m^3$ at $f_s = 100kHz$, $B_{max} = 150mT$. Finally, resistance of the primary, secondary and tertiary winding of the three-winding transformer were measured using the impedance analyzer and estimated accordingly for the OBC and APM transformers based on the core dimensions and design specifications.

TABLE X
Design Parameters For Integrated And Separate OBC-APM Transformers

Parameter	Symbol	Integrated	OBC	APM
Primary winding RMS current	$I_{1,rms}$	13A	10A	2.5A
Secondary winding RMS current	$I_{2,rms}$	11.5A	10A	50A
Tertiary winding RMS current	$I_{3,rms}$	50A	-	-
Peak magnetic flux	B_{max}	$150mT$		
Switching frequency	f_s	$100kHz$		
Current density	J	$4A/mm^2$		
Fill factor - Litz	k_1	0.15		
Fill factor - Foil	k_2	0.4		

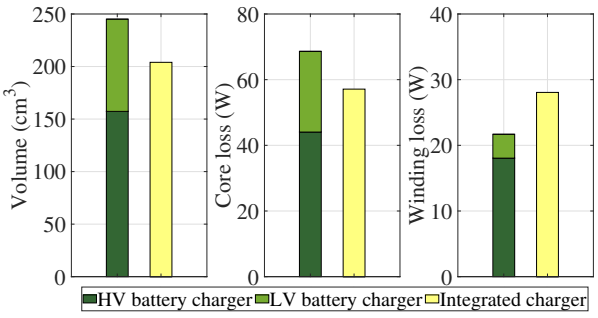

Fig. 36. Total volume, magnetic core loss and winding copper loss comparison between the transformers of the separate HV and LV battery chargers and the integrated one.

According to Fig. 36, 16.7% reduction of the transformer volume can be achieved with the proposed integrated three-winding transformer, compared to the individual ones. Since magnetic core loss is proportional to the volume of the magnetic core, transformer core loss can also be reduced by 16.7% in the case of the three-winding transformer. Although winding loss of the integrated transformer is increased by 28%, total power loss of the integrated transformer can be reduced by 6% compared to the separate DAB and PSFB transformers.

A comparison between the proposed integrated charger and existing chargers in the literature is shown in Table XI. The proposed integrated charger is capable of simultaneous HV and LV battery charging in contrast to the integrated chargers presented in [6] and [17]. Moreover, isolation requirements between the grid and the HV battery as well as the HV and LV battery are ensured due to the use of the three-winding transformer. The latter reduces the total volume and cost of the integrated charger compared to the use of two-winding

TABLE XI
Comparison With Existing Chargers

Charger	Proposed	[6]	[11]	[13]	[14]	[17]	[18]	[35], [40]
OBC-APM topology	DAB-PSFB	DAB-DAB & Buck	Full bridge-LLC	LLC-PSFB	DAB-Buck	LLC-LLC	CFTAB	Separate DAB
Simultaneous charging	Yes	No	Yes	Yes	Yes	No	Yes	-
Isolation	Yes	Yes	No	Yes	Yes	Yes	Yes	Yes
Mechanical switches	No	Yes	Yes	No	No	No	No	No
Active switches	8	8	6	10	9	10	12	16
Diodes	4	0	2	0	3	0	0	0
Transformer	3-winding	2-winding	3-winding	2 x 2-winding	3-winding	3-winding	3-winding	2 x 2-winding
Nominal power (kW)	3.3/0.5	0.7	2/0.5	3.3/0.4	3/0.3	3.3	11/3.5	3.7/2
Efficiency (%)	94	-	95.7	97.7	94	-	-	94.2

transformers [13], [35], [40]. Moreover, the chargers described in [6], [11] rely on mechanical switches which raises reliability concerns. On the other hand, the proposed charger can support all operation modes without the need of mechanical switches or relays. Finally, the efficiency of the proposed converter is presented in Table XI for nominal power operation and the case where port 3 utilizes diodes instead of the synchronous rectification scheme. It is shown that the proposed converter can achieve high efficiency, while at the same time the number of active switches can be significantly reduced, compared to most of the existing chargers of Table XI. Hence, control complexity is improved, while also cost is reduced due to the need of less low-power control electronics.

VII. Conclusions

An isolated three-port DC-DC converter has been presented and analyzed in this paper. The proposed converter is suitable for OBC and APM integration in the EV powertrain and is capable of charging both HV and LV batteries simultaneously, operating over a wide voltage range. Moreover, the proposed converter does not rely on mechanical switches or relays. A single three-winding transformer is utilized to meet isolation requirements, which reduces the volume and cost of the magnetics compared to the use of separate two-winding transformers. A boundary condition has been derived and a novel modulation scheme has been proposed to decouple the power flow between the converter three ports and allow independent charging of the HV and LV batteries. In addition, a converter 3-degrees-of-freedom selection scheme has been proposed and as a result ZVS is achieved for all active devices of the converter over wide power and voltage range, without the need of additional resonant components. The experimental results of a SiC MOSFET converter prototype proved the effectiveness of the proposed converter for future integrated OBC application.

References

[1] J. Yuan, L. Dorn-Gomba, A. D. Callegaro, J. Reimers, and A. Emadi, "A review of bidirectional on-board chargers for electric vehicles," *IEEE Access*, vol. 9, pp. 51 501–51 518, 2021.

[2] R. Hou, P. Magne, B. Bilgin, and A. Emadi, "A topological evaluation of isolated dc/dc converters for auxiliary power modules in electrified vehicle applications," in *2015 IEEE Applied Power Electronics Conference and Exposition (APEC)*, 2015, pp. 1360–1366.

[3] A. K. Singh and M. K. Pathak, "A comprehensive review of integrated charger for on-board battery charging applications of electric vehicles," in *2018 IEEE 8th Power India International Conference (PIICON)*, 2018, pp. 1–6.

[4] A. Khaligh and M. D'Antonio, "Global trends in high-power on-board chargers for electric vehicles," *IEEE Transactions on Vehicular Technology*, vol. 68, no. 4, pp. 3306–3324, 2019.

[5] B. Khasawneh, M. Sabra, and M. Zohdy, "Novel operating mode for dc-to-dc converters in phevs," SAE Technical Paper, Tech. Rep., 2013.

[6] S. Kim and F.-S. Kang, "Multifunctional onboard battery charger for plug-in electric vehicles," *IEEE Transactions on Industrial Electronics*, vol. 62, no. 6, pp. 3460–3472, 2015.

[7] H. V. Nguyen and D.-C. Lee, "Advanced single-phase onboard chargers with small dc-link capacitors," in *2018 IEEE International Power Electronics and Application Conference and Exposition (PEAC)*, 2018, pp. 1–6.

[8] H. V. Nguyen, D.-D. To, and D.-C. Lee, "Onboard battery chargers for plug-in electric vehicles with dual functional circuit for low-voltage battery charging and active power decoupling," *IEEE Access*, vol. 6, pp. 70 212–70 222, 2018.

[9] H. V. Nguyen and D.-C. Lee, "Single-phase multifunctional onboard battery chargers with active power decoupling capability," in *2018 IEEE Applied Power Electronics Conference and Exposition (APEC)*, 2018, pp. 3434–3439.

[10] ——, "An improved low-voltage charging circuit for single-phase onboard battery chargers," in *2019 IEEE Applied Power Electronics Conference and Exposition (APEC)*, 2019, pp. 3325–3331.

[11] H. V. Nguyen, D.-C. Lee, and F. Blaabjerg, "A novel sic-based multifunctional onboard battery charger for plug-in electric vehicles," *IEEE Transactions on Power Electronics*, vol. 36, no. 5, pp. 5635–5646, 2021.

[12] D.-H. Kim, M.-J. Kim, and B.-K. Lee, "An integrated battery charger with high power density and efficiency for electric vehicles," *IEEE Transactions on Power Electronics*, vol. 32, no. 6, pp. 4553–4565, 2017.

[13] G. Yu and S. Choi, "An effective integration of apm and obc with simultaneous operation and entire zvs range for electric vehicle," *IEEE Transactions on Power Electronics*, vol. 36, no. 9, pp. 10 343–10 354, 2021.

[14] Y.-S. Kim, C.-Y. Oh, W.-Y. Sung, and B. K. Lee, "Topology and control scheme of obc–ldc integrated power unit for electric vehicles," *IEEE Transactions on Power Electronics*, vol. 32, no. 3, pp. 1731–1743, 2017.

[15] H. Ma, Y. Tan, L. Du, X. Han, and J. Ji, "An integrated design of power converters for electric vehicles," in *2017 IEEE 26th International Symposium on Industrial Electronics (ISIE)*, 2017, pp. 600–605.

[16] I. Kougioulis, P. Wheeler, and M. R. Ahmed, "An integrated on-board charger and auxiliary power module for electric vehicles," in *2022 IEEE Applied Power Electronics Conference and Exposition (APEC)*, 2022, pp. 1162–1169.

[17] Y. Tang, J. Lu, B. Wu, S. Zou, W. Ding, and A. Khaligh, "An integrated dual-output isolated converter for plug-in electric vehicles," *IEEE Transactions on Vehicular Technology*, vol. 67, no. 2, pp. 966–976, 2018.

[18] L. Zhu, H. Bai, A. Brown, and L. Keuck, "A current-fed three-port dc/dc converter for integration of on-board charger and auxiliary power module in electric vehicles," in *2021 IEEE Applied Power Electronics Conference and Exposition (APEC)*, 2021, pp. 577–582.

[19] C. Zhao, S. D. Round, and J. W. Kolar, "An isolated three-port bidirectional dc-dc converter with decoupled power flow management," *IEEE Transactions on Power Electronics*, vol. 23, no. 5, pp. 2443–2453, 2008.

[20] H. Tao, A. Kotsopoulos, J. L. Duarte, and M. A. M. Hendrix, "Transformer-coupled multiport zvs bidirectional dc–dc converter with wide input range," *IEEE Transactions on Power Electronics*, vol. 23, no. 2, pp. 771–781, 2008.

[21] S. Dey and A. Mallik, "Multivariable-modulation-based conduction loss minimization in a triple-active-bridge converter," *IEEE Transactions on Power Electronics*, vol. 37, no. 6, pp. 6599–6612, 2022.

[22] P. Wang, X. Lu, W. Wang, and D. Xu, "Frequency division based coordinated control of three-port converter interfaced hybrid energy storage systems in autonomous dc microgrids," *IEEE Access*, vol. 6, pp. 25 389–25 398, 2018.

[23] H. Krishnaswami and N. Mohan, "Three-port series-resonant dc–dc converter to interface renewable energy sources with bidirectional load and energy storage ports," *IEEE Transactions on Power Electronics*, vol. 24, no. 10, pp. 2289–2297, 2009.

[24] N. D. Dao, D.-C. Lee, and Q. D. Phan, "High-efficiency sic-based isolated three-port dc/dc converters for hybrid charging stations," *IEEE Transactions on Power Electronics*, vol. 35, no. 10, pp. 10 455–10 465, 2020.

[25] Z. Lin, S. Pan, M. Wang, W. Lin, J. Gong, L. Yao, and P. Jain, "A three-port lcc resonant converter for the 380-v/48-v hybrid dc system," *IEEE Transactions on Power Electronics*, vol. 37, no. 9, pp. 10 864–10 876, 2022.

[26] "Electric vehicle (ev) drivetrain system," https://www.infineon.com/cms/en/applications/automotive/electric-drive-train/, accessed: 2021-04-04.

[27] R. Erickson and D. Maksimovic, *Fundamentals of Power Electronics*, 01 2020.

[28] S. Bandyopadhyay, P. Purgat, Z. Qin, and P. Bauer, "A multiactive bridge converter with inherently decoupled power flows," *IEEE Transactions on Power Electronics*, vol. 36, no. 2, pp. 2231–2245, 2021.

[29] T. Mishima, K. Akamatsu, and M. Nakaoka, "A high frequency-link secondary-side phase-shifted full-range soft-switching pwm dc–dc converter with zcs active rectifier for ev battery chargers," *IEEE Transactions on Power Electronics*, vol. 28, no. 12, pp. 5758–5773, 2013.

[30] D.-D. Tran, H.-N. Vu, S. Yu, and W. Choi, "A novel soft-switching full-bridge converter with a combination of a secondary switch and a nondissipative snubber," *IEEE Transactions on Power Electronics*, vol. 33, no. 2, pp. 1440–1452, 2018.

[31] C.-Y. Lim, J.-K. Han, M.-H. Park, K.-W. Kim, and G.-W. Moon, "Phase-shifted full-bridge dc-dc converter with high efficiency and reduced output filter using center-tapped clamp circuit," in *2019 IEEE Applied Power Electronics Conference and Exposition (APEC)*, 2019, pp. 1710–1715.
[32] B. Zhao, Q. Song, W. Liu, and Y. Sun, "Overview of dual-active-bridge isolated bidirectional dc–dc converter for high-frequency-link power-conversion system," *IEEE Transactions on Power Electronics*, vol. 29, no. 8, pp. 4091–4106, 2014.
[33] P. Purgat, S. Bandyopadhyay, Z. Qin, and P. Bauer, "Zero voltage switching criteria of triple active bridge converter," *IEEE Transactions on Power Electronics*, vol. 36, no. 5, pp. 5425–5439, 2021.
[34] B. Zhao, Q. Song, W. Liu, G. Liu, and Y. Zhao, "Universal high-frequency-link characterization and practical fundamental-optimal strategy for dual-active-bridge dc-dc converter under pwm plus phase-shift control," *IEEE Transactions on Power Electronics*, vol. 30, no. 12, pp. 6488–6494, 2015.
[35] F. Krismer and J. W. Kolar, "Closed form solution for minimum conduction loss modulation of dab converters," *IEEE Transactions on Power Electronics*, vol. 27, no. 1, pp. 174–188, 2012.
[36] R. De Doncker, D. Divan, and M. Kheraluwala, "A three-phase soft-switched high power density dc/dc converter for high power applications," in *Conference Record of the 1988 IEEE Industry Applications Society Annual Meeting*, 1988, pp. 796–805 vol.1.
[37] Y. Wu, M. H. Mahmud, S. Christian, R. A. Fantino, R. A. Gomez, Y. Zhao, and J. C. Balda, "A 150-kw 99x0025; efficient all-silicon-carbide triple-active-bridge converter for solar-plus-storage systems," *IEEE Journal of Emerging and Selected Topics in Power Electronics*, vol. 10, no. 4, pp. 3496–3510, 2022.
[38] V.-B. Vu, D.-H. Tran, and W. Choi, "Implementation of the constant current and constant voltage charge of inductive power transfer systems with the double-sided lcc compensation topology for electric vehicle battery charge applications," *IEEE Transactions on Power Electronics*, vol. 33, no. 9, pp. 7398–7410, 2018.
[39] A. J. Hanson and D. J. Perreault, "Modeling the magnetic behavior of n-winding components: Approaches for unshackling switching superheroes," *IEEE Power Electronics Magazine*, vol. 7, no. 1, pp. 35–45, 2020.
[40] J. Everts, F. Krismer, J. Van den Keybus, J. Driesen, and J. W. Kolar, "Optimal zvs modulation of single-phase single-stage bidirectional dab ac–dc converters," *IEEE Transactions on Power Electronics*, vol. 29, no. 8, pp. 3954–3970, 2014.

Ioannis Kougioulis received the M.Eng. degree from the Electrical and Computer Engineering Department of the University of Patras, Greece, in 2018. He is currently working towards the Ph.D. degree with the Power Electronics, Machines and Control (PEMC) Research Group of the University of Nottingham, UK. His research interests include high-frequency DC-DC converters, multiport converters and high-frequency magnetics.

Anirban Pal (Member, IEEE) received the B.E. degree from the Indian Institute of Engineering Science and Technology, Shibpore, India, in 2010, the M.E. and the Ph.D. degree from the Indian Institute of Science, Bangalore, India, in 2015 and in 2020 respectively, all in electrical engineering.

From 2010 to 2013, he was an Assistant Manager with the National Thermal Power Corporation Limited. From 2020 to 2022 he was a postdoctoral research associate with the Power Electronics Machines and Control (PEMC) Research Group of the University of Nottingham, UK. He is currently working as a lead engineer at GE Aerospace, Bangalore, India. His research interests include high frequency-link single stage converters, dual active bridge based converters, resonant converters, soft-switching techniques, and design of high-frequency magnetics.

Patrick Wheeler (Fellow, IEEE) received the B.Eng. (Hons.) degree in power electronics and the Ph.D. degree in electrical engineering for his work on matrix converters from the University of Bristol, Bristol, U.K., in 1990 and 1994, respectively. In 1993, he moved to the University of Nottingham and worked as a Research Assistant with the Department of Electrical and Electronic Engineering. In 1996, he became a Lecturer with the Power Electronics, Machines and Control Group, University of Nottingham, U.K., where he has been a Full Professor since January 2008. He is currently the Global Engagement Director with the Faculty of Engineering, the Head of the Power Electronics, Machines and Control Research Group, and the Director of the University of Nottingham's Institute of Aerospace Technology. He was the Head of the Department of Electrical and Electronic Engineering, University of Nottingham, from 2015 to 2018. He has authored and co-authored more than 850 academic publications in leading international conferences and journals. Prof. Wheeler is a member of the IEEE PELs AdCom and is currently IEEE PELS Vice-President for Technical Operations.

Md Rishad Ahmed (Member, IEEE) received the B.Sc. degree from the Bangladesh University of Engineering and Technology (BUET), Dhaka, Bangladesh in 2011, and the M.Sc. degree (with Distinction) and the Ph.D. degree from the University of Manchester, Manchester, U.K., in 2013 and 2017, respectively. Prior to joining University of Nottingham as an Assistant Professor in 2020, he worked as a design engineer at Dynex Semiconductor, U.K for 2.5 years. His research interests include high-frequency converters, wideband-gap semiconductor devices, passive components, and converter packaging.